ORNL/TM-2025/4137

Development and Evaluation of Embrittlement Resistant Alloys for Advanced LWR Cladding

Caleb Massey
Annabelle Le Coq
Jesse Werden
Ethan Blount
David Collins
Anthony Guajardo
Nick Russell
David Hoelzer
Sebastien Dryepondt
Yukinori Yamamoto
Richard Howard
Thomas Siggillino
Kory Linton

September 2025
M2FT-25OR080202011

OAK RIDGE National Laboratory

ORNL/TM-2025/4137

Advanced Fuels Campaign

Development and Evaluation of Embrittlement Resistant Alloys for Advanced LWR Cladding

Caleb Massey
Annabelle Le Coq
Jesse Werden
Ethan Blount
David Collins
Anthony Guajardo
Nick Russell
David Hoelzer
Sebastien Dryepondt
Yukinori Yamamoto
Richard Howard
Thomas Siggillino
Kory Linton

September 2025

M2FT-25OR080202011

Prepared by
OAK RIDGE NATIONAL LABORATORY
Oak Ridge, TN 37831
managed by
UT-BATTELLE LLC
for the
US DEPARTMENT OF ENERGY
under contract DE-AC05-00OR22725

CONTENTS

LIST OF FIGURES

LIST OF TABLES

ABBREVIATIONS

AFA	alumina-forming austenitic alloy
AFF	AFC FeCrAl fracture
AFT	AFC FeCrAl tensile
AMOW	Additively Manufactured, ODS, and Wrought
ATF	accident tolerant fuel
BCC	body-centered cubic
CR	cold-rolled
DOE	Department of Energy
EBSD	electron backscatter diffraction
FCC	face-centered cubic
GENTEN	general tensile
HIP	hot-isostatic pressing
HR	hot-rolled
IMET	Irradiated Materials Examination and Testing
IPF	inverse pole figure
LOCA	loss-of-coolant accident
LT-ATF	Long Term Accident Tolerant Fuel
LWR	light water reactor
MINBEN	miniature bend bar
ORNL	Oak Ridge National Laboratory
PM	powder metallurgical
SMR	small modular reactor
TE	total elongation
UE	uniform elongation
UTS	ultimate tensile strength
VIM	vacuum induction melting
YS	yield strength

ACKNOWLEDGMENTS

This research was sponsored by the Advanced Fuels Campaign (AFC) within the US Department of Energy (DOE), Office of Nuclear Energy. Neutron irradiation in the High Flux Isotope Reactor (HFIR) is made possible by the Office of Basic Energy Sciences, US DOE. The report was authored by UT-Battelle, LLC under Contract No. DE-AC05-00OR22725 with the US Department of Energy. The authors thank Jerid Metcalf, Clay Morris, and the Irradiated Materials Examination and Testing hot cell facility staff for their help during the post-irradiation examination of these experiments. We would also like to thank Jim Horenburg for assistance with unirradiated metallography support. Finally, we would like to thank and acknowledge Stephen Taller and Sam Bell for their thoughtful reviews of this report.

SUMMARY

The primary challenge preventing the deployment of reactor designs that leverage wrought FeCrAl as an advanced light-water reactor (LWR) cladding is irradiation hardening and embrittlement. Wrought FeCrAl alloys experience a loss of post-irradiation ductility and fracture toughness under low-temperature neutron irradiation (< 350°C) resulting from the combined effects of dislocation loop formation and the irradiation-enhanced precipitation of Cr-rich alpha-prime precipitates throughout the microstructure. Over the past decade, significant improvements in our understanding regarding the effect of Cr and Al content have been enabled through neutron irradiations, but even optimized wrought alloys such as C26M remain vulnerable to brittle failure during storage, transportation, and handling following irradiation.

This report summarizes multiple irradiation campaigns initiated over the past 7 years and provides recent insights into the effect of (1) minor alloying composition, (2) alloy processing strategy, (3) crystal structure, and (4) the use of advanced oxide dispersion strengthened (ODS) alloys. The first irradiation campaign irradiated body-centered cubic FeCrAl alloy C26M with and without elements such as Mo and Y. It also included face-centered cubic alumina-forming austenitic (AFA) alloys that have a steeper neutronic penalty but that have far superior high-temperature strength than wrought FeCrAl. Finally, this campaign compared conventional wrought C26M with the same material produced using modern powder metallurgical hot-isostatic pressing (PM-HIP). The second irradiation campaign, initiated in 2018, irradiated wrought and FeCrAl-ODS materials up to 50 dpa to assess their irradiation resistance to high-doses.

The results of this work indicate that wrought C26M suffers significant degradation following neutron irradiation at LWR-relevant temperatures regardless of Mo and Y content. The PM-HIP variant appears to be more resilient to irradiation-induced ductility loss in comparison with wrought variants but still loses almost all ductility by 8 dpa. Notably, the AFAs retained at least 5% total elongation after irradiation at the same dose and temperature condition, although additional deterioration may be expected at higher fluence levels.

FeCrAl-ODS materials show the greatest promise as a transformative longer-term accident-tolerant fuel (LT-ATF) cladding material. The extruded 106ZY10C alloy retained 10% total elongation after 16 dpa irradiation and retained 8% total elongation after 50 dpa. Additional challenges with FeCrAl-ODS alloys also remain, including optimization of end cap joining methodologies, enhancement of fracture toughness, scaling production to prove economic viability, and optimizing post-pilger heat treatments to maximize ductility and irradiation resistance.

This series of irradiations demonstrates the efficacy of the LWR testbed available within the United States for the rapid irradiation and down-selection of LT-ATF candidates. As the country rapidly accelerates its timeline for the deployment of advanced reactor concepts, the effective utilization of the High Flux Isotope Reactor for separate-effects style irradiations should continue to be prioritized to answer the final questions pertaining to LT-ATF candidates necessary for the deployment of advanced boiling water reactors and small modular reactors.

1. INTRODUCTION

FeCrAl alloys have been a candidate for accident-tolerant fuel (ATF) cladding since a technology implementation plan was developed for this class of alloys in 2014 by Oak Ridge National Laboratory (ORNL) [1]. Over the past 10 years, significant tensile and fracture toughness data as a function of temperature and dose have been generated on model FeCrAl alloys with respect to various chromium and aluminum alloy compositions, as well as varied grain structures [2-8]. The FeCrAl alloys consistently show significant irradiation hardening and embrittlement at irradiation temperatures below 300°C, effects that are associated with high densities of irradiation-induced defects (dislocation loops/black dots) and irradiation-enhanced precipitation (chromium-rich alpha prime phase precipitation).

Due to the complexity of the initial irradiations and the rapid iteration of compositions and microstructures during the initial irradiation campaigns, gaps in our understanding still remain about the effect of (1) minor alloying elements, (2) processing effects, 3) crystal structure, and (4) sink strength on the fundamental resistance of FeCrAl alloys to irradiation hardening and embrittlement.

In FY24, an irradiation campaign was undertaken to address questions (1) and (2) above, whereby the popular low-Cr FeCrAl alloy C26M (nominal composition Fe-12Cr-6Al-2Mo) was produced using conventional arc melting and thermomechanical processing (wrought material) with and without minor alloying additions. In addition to varied minor alloying for C26M, the same material was produced using modern powder metallurgical hot-isostatic pressing (HIP) methods to explore effects of novel processing routes. To understand the effects of (2) crystal structure face-centered cubic (FCC) variants of alumina-forming austenitic (AFA) alloys were also produced and irradiated alongside the conventional body-centered cubic (BCC) variants to assess their irradiation response after simulated light-water reactor (LWR) neutron irradiation conditions. These AFAs were initially developed for fossil applications [9] but are increasingly popular in commercial nuclear power as potential alloys for lead-cooled fast reactor structural materials [10]. Due to their high chromium content and aluminum content, they may provide competitive corrosion and oxidation performance in the presence of high-temperature water/steam as well. Finally addressing sink strength effects (3), prior irradiations of wrought and FeCrAl-ODS alloys to doses up to 50 dpa at LWR-relevant temperatures were completed in FY25 and have now allowed us to probe the retained ductility of advanced variants of FeCrAl alloys with high sink strength as a means to resist hardening and embrittlement.

This year, Oak Ridge National Laboratory completed targeted post-irradiation examination on these FeCrAl, FeCrAl-ODS, and AFA compositions. The resulting data represent doses as high as 8 dpa for the FeCrAl and AFA compositions as well as doses as high as 50 dpa for advanced FeCrAl-ODS material, which corresponds to doses relevant for LWR and small modular reactors (SMRs), respectively. This report summarizes pertinent mechanical property data from room-temperature mechanical tests on these alloys to provide insight into potential research pathways to improve the irradiation hardening and embrittlement resistance of these longer-term accident-tolerant fuel (LT-ATF) candidates.

2. MATERIALS AND METHODS

2.1 CANDIDATE MATERIALS OF INTEREST

In this section, the materials of interest and their respective processing are described, followed by a discussion of the various irradiation campaigns and the materials included in each one. The baseline alloy characterized in this work is the FeCrAl alloy C26M, with nominal composition (Fe-12Cr-6Al-2Mo-0.2Si+0.05Y wt%). This alloy was down-selected as an initial ATF cladding candidate due to its superior high-temperature steam oxidation resistance in comparison to that of reference Zr-based alloys [11, 12], as well as for its superior mechanical strength at elevated temperatures [13-15]. Other materials include C26M variants with minor differences in thermomechanical processing and/or composition, as well as oxide dispersion strengthened (ODS) and/or FCC AFA materials. The materials discussed in this work are listed below in Table 1.

Table 1. FeCrAl, FeCrAl-ODS and AFA alloys included in AFT, AFF, and/or AMOW rabbits.

Alloy family	Alloy	Description/Reference	Nominal Composition (wt%)	SSJ-2 specimen	MBS-1 specimen
FeCrAl	C26M-HR	Conventional, Hot-Rolled	Fe-12Cr-6Al-2Mo+0.2Si+0.04Y	✓	
	C26M-WR	Conventional, Hot Rolled + Warm Rolled	Fe-12Cr-6Al-2Mo+0.2Si+0.05Y	✓	
	C26M4	Conventional, Rolled and Annealed / [16]	Fe-12Cr-6Al-2Mo+0.2Si+0.03Y	✓	✓
	C26M-HIP	Hot-isostatically pressed / [16]	Fe-12Cr-6Al-2Mo+0.2Si	✓	
	C26M-0Y	Y-free Variant / [16]	Fe-12Cr-6Al-2Mo+0.2Si	✓	✓
	B126N	Mo-free Variant / [16]	Fe-12Cr-6Al+0.2Si	✓	
FeCrAl-ODS	106ZY10C	[17, 18]	Fe-10Cr-6.1Al-0.3Zr+0.3Y2O3	✓	
AFA	AA06	heat #21831 / [16]	Fe-25Ni-16Cr-4Al-2Mo-0.6Nb-0.2Si-0.2Mn-0.03C-0.03Y	✓	✓
	AA07	heat #21832 / [16]	Fe-25Ni-16Cr-4Al-2Mo-1.0Nb-0.2Si-0.2Mn-0.03C-0.03Y	✓	✓
	AA09	heat #21834 / [16]	Fe-25Ni-16Cr-4Al-2Mo-2.5Nb-0.2Si-0.2Mn-0.03C-0.03Y	✓	✓

2.1.1 Wrought and Powder-Metallurgical FeCrAl

Regarding baseline C26M-type FeCrAl alloys, there are three nominal C26M materials, spanning two heats and three thermomechanical processing treatments. Table 1 lists three initial FeCrAl alloys: C26M-HR, C26M-WR, and C26M4. The first two of these alloys, C26M-HR, and C26M-WR were fabricated using vacuum induction melting (VIM) to produce an initial ingot of material with a 4.25" diameter and a length of 21". The material was subjected to HIP at 1200°C and 100 MPa, followed by hot forging at 1100°C from a thickness of 0.75 in. to 0.2 in. The resulting bar was given two final processing paths, resulting in either a final hot-rolled (HR) or warm-rolled (WR) microstructure. Hot rolling was performed at 800°C to a final plate thickness of 0.03", and the resulting bar is C26M-HR. The C26M-WR material is the same plate as the C26M-HR but with a final additional warm-rolling step at 300°C from 0.03 in. thick to 0.025" thick. The characteristic microstructures observed for these two plates are shown in Figure 1.

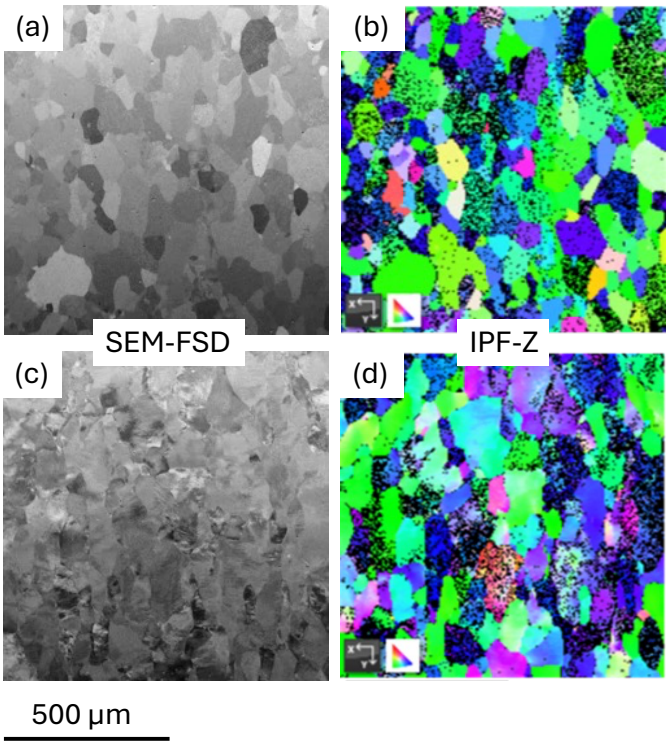

Figure 1. Scanning electron forward scattering detector (SEM-FSD) and electron backscatter diffraction inverse pole figure (EBSD-IPF) maps of C26M-HR (a-b) and C26M-WR (c-d) plates.

The other C26M4 plate was produced through vacuum induction melting at an external shop (Sophisticated Alloys, Inc.), delivered as ~80 lb columnar-shaped ingot with a 4 in. diameter. This plate was hot-rolled with multiple passes, targeting 15% reduction per pass until a final plate thickness of 0.25 in. was produced. After hot-rolling, the sheet was flattened and then subjected to a final annealing treatment at 900°C for 30 min.

The C26M-0Y material was produced without added Y-content to assess the effect of secondary intermetallic precipitates commonly identified on grain boundaries within the FeCrAl alloy that

have been known to be amorphized under irradiation [19]. The C26M-0Y was produced as a drop-casted ingot in a 1” × 1” × 5” geometry, where the middle 2.5” segment was sectioned for specimen production. The ingot was homogenized via heat treatment at 1200°C with argon cover gas followed by air cooling to room temperature. The ingots were then soaked at 800°C in air for 30 min, followed by hot-pressing along the longitudinal axis. The ingot was then hot-rolled and annealed in the same manner as C26M4. The B126N material is identical in processing pathway to C26M-0Y and represents the C26M composition without either Y or Mo added to the microstructure.

The final alloy of interest in the FeCrAl category is C26M-HIP; it has the same nominal composition as that of C26M-0Y but is fabricated using the HIP process rather than by conventional melting, forging, and rolling processes. The source powder was procured from Powder Alloy Corporation (heat# PAC2603), and HIP was performed at 1050°C for 3 h at 150 MPa to achieve a fine grain size and full densification. This was a highly pure powder, with an O content of only 110 ppmw, with a particle size distribution ranging from 10-100 µm.

The microstructures of C26M4 (baseline annealed), C26M-HIP, C26M-0Y (no yttrium), and B126N (no yttrium or molybdenum) are shown in Figure 2. The C26M4 material has a recrystallized microstructure with a coarse grain structure averaging approximately 100 µm in diameter. Conversely, the C26M-HIP material has a much finer equiaxed grain size below ~20 µm in diameter. The B126N and C26M-0Y materials, on the other hand, have a large columnar grain structure when subjected to the same heat treatment as C26M4, as the lack of either Mo, Y, or both resulted in differences in recrystallization and/or grain growth kinetics. This is considered a non-optimized microstructure, but relative differences in irradiation performance can still be ascertained from a comparison of these four alloys.

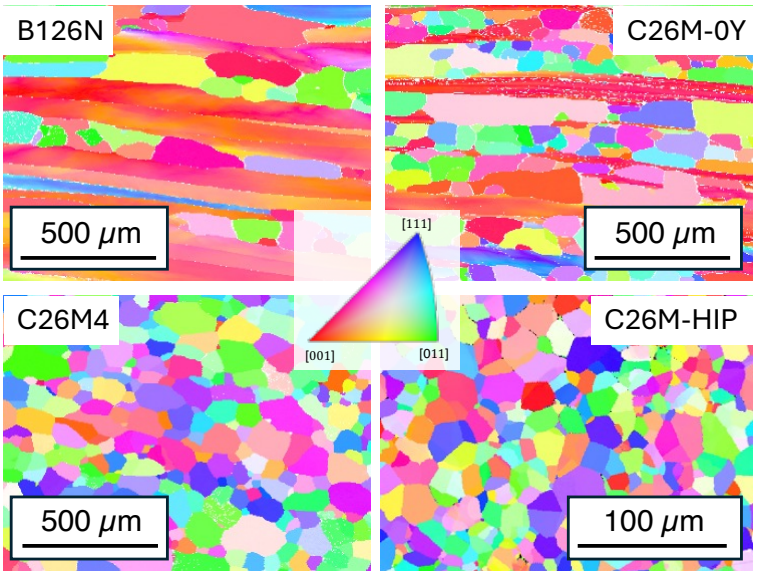

Figure 2. EBSD IPF maps of plate materials for B126N, C26M-0Y, C26M4, and C26M-HIP, reproduced from [16]. Prior rolling direction (for wrought materials) is oriented horizontally in the image.

2.1.2 Oxide Dispersion Strengthened (ODS) FeCrAl

The FeCrAl-ODS material investigated in this work has been extensively documented in prior literature funded by the AFC program [17, 20-29], but the processing steps are briefly summarized here. The alloy investigated (106ZY10C) was produced via the mechanical alloying of low-Cr gas atomized FeCrAl powder with 0.3 wt.% nanocrystalline yttria powder to produce a final alloy with nominal composition Fe-10Cr-6.1Al-0.3Zr-0.3Y_2O_3. The powder was ball-milled under an Ar environment for 40 h in a Zoz Simoloyer CM01, followed by canning and degassing for 24 h at 300°C. The final rod was produced via extrusion at 1000°C following a 1 h hold at the same temperature. The other name used in the literature for this alloy is 4H10C [17].

The general microstructure of 106ZY10C consists of a bimodal distribution of sub-micron grains as well as larger columnar grains with significant intragranular orientation spread due to the high dislocation content within the alloy, as shown in Figure 3(a). The grain structure and the high dislocation density are stabilized via a similarly high density of nanoscale precipitates that serve as pinning sites for both grain boundaries and dislocations within the microstructure. In this particular alloy, the precipitates have been shown to be a mixture of various ternary phases of Y-Al-O, with average sizes in the 2–4 nm range [20].

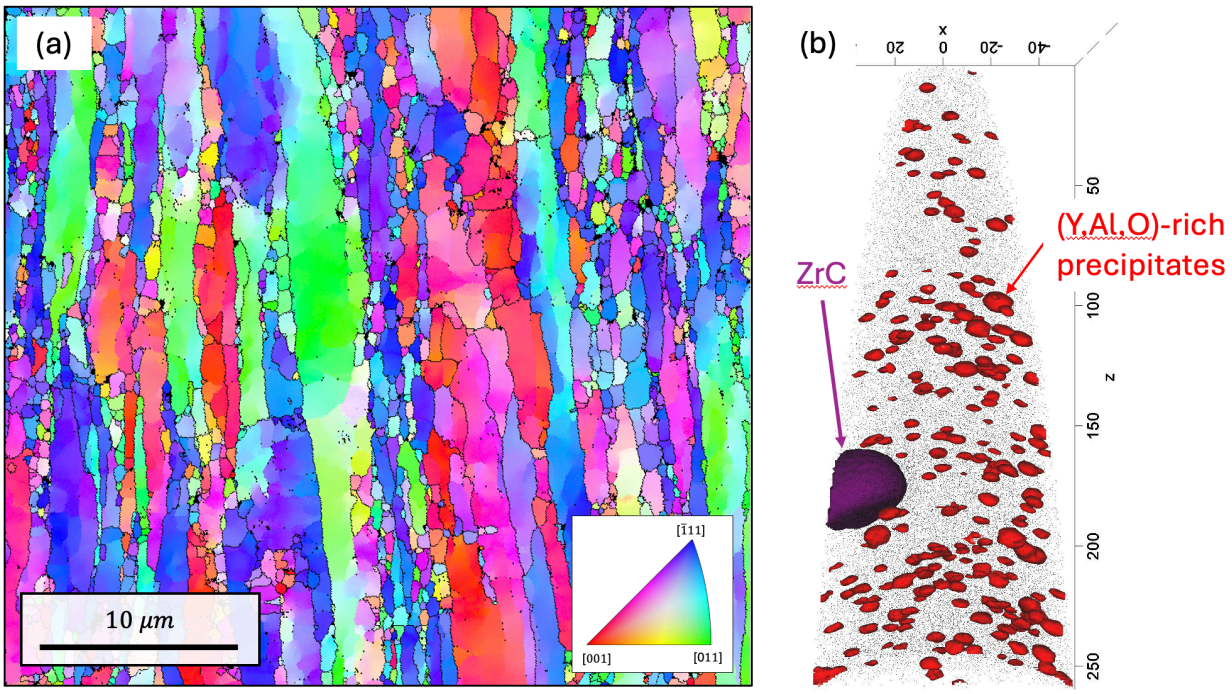

Figure 3. Representative microstructure of 106ZY10C. Shown via (a) an EBSD-IPF map (reproduced from [17]), as well (b) an atom probe tomography (APT) isosurface map indicating the presence of Y-Al-O rich precipitates (red) and Zr-rich carbides (purple), reproduced from [20].

2.1.3 Alumina-Forming Austenitic (AFA) Alloys

In the event that neither thermomechanical processing nor compositional optimization could help alleviate the ductility loss associated with FeCrAl irradiation hardening and embrittlement, a new class of alumina-forming alloys with an FCC crystal structure was also scoped in the current set

of irradiations. These AFAs are a family of stainless steels to which aluminum and other chemical elements have been added to the matrix to enhance their high-temperature corrosion and oxidation performance.

For the AFC program, a specific series of AFC AFAs (designated AA##) were produced to establish whether a specific compositional regime existed that results in stable aluminum-oxide scale formation at temperatures relevant to loss-of-coolant accident (LOCA) scenarios. The compositions of these alloys are quite complex, as some elements such as Cr and Al are strong ferrite stabilizers, and must be counteracted with sufficient contents of austenite stabilizing elements. As such, to add sufficient Cr and Al levels for corrosion and oxidation resistance, elements such as Ni and Mn were needed to stabilize the FCC structure. This is why this series of AFAs, with 16 wt% Cr and 4 wt% Al, also contained 25 wt% Ni and 0.2 wt% Mn. This creates three potential problems for the AFAs: (1) high neutron absorption cross section of 2.8 b vs. 2.3 b for BCC FeCrAl, (2) open questions regarding the extent of radioactive corrosion products with such high Ni content within the material, and (3) potential embrittlement due to Ni transmutation and subsequent He production. This work focuses on the third issue; the other two are beyond the scope of the current work.

Three AA-series AFAs (Figure 4) were down-selected for this irradiation campaign, all with the same nominal composition (Fe-25Ni-16Cr-4Al-2Mo-0.2Si-0.2Mn-0.03C-0.03Y-(0.6-2.5)Nb) but with three increasing Nb-contents of 0.6 wt% Nb (AA06), 1.0 wt% Nb (AA07), and 2.5 wt% Nb (AA09). The increasing Nb content has been shown to not only increase the volume fraction of strengthening carbides, but also the oxidation resistance of AFAs at high temperature [30].

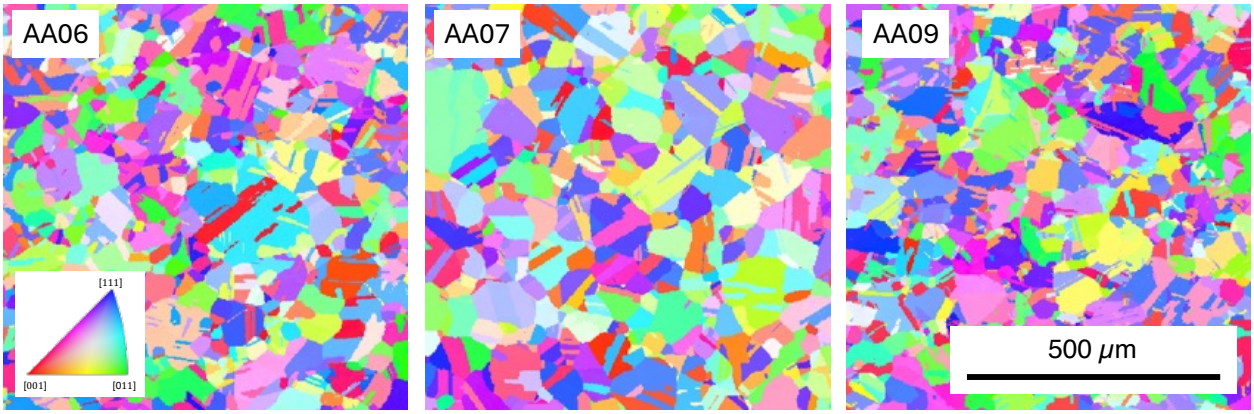

Figure 4. Representative EBSD grain structures of each AFA evaluated in the current irradiation campaign, including (a) AA06, (b) AA07, and (c) AA09, reproduced from [16]

2.2 IRRADIATION CAMPAIGNS TARGETING IRRADIATION HARDENING & EMBRITTLEMENT

2.2.1 AFC FeCrAl Tensile (AFT) and AFC FeCrAl Fracture (AFF)

The first of two irradiation campaigns discussed in this report is the combined AFC FeCrAl Tensile (AFT) and Fracture (AFF) campaign of both BCC and FCC alumina forming Fe-based alloys. This campaign is summarized in a previous report [16]. This irradiation campaign was meant to establish the difference between the performance of the FeCrAl alloys and AFAs under low- to intermediate-dose neutron irradiation, with a target temperature of 315°C and two target irradiation doses (2 dpa and 8 dpa).

For this irradiation campaign, two different rabbit designs were leveraged [31]. First, the standardized general tensile (GENTEN) rabbit, illustrated in Figure 5, was used to probe effects of irradiation on strength and retained ductility in each alloy. In parallel, a new miniature bend-bar (MINBEN) rabbit was used, shown in Figure 6, which allows for the direct measurement of the resistance of each material to crack propagation before and after irradiation. A total of four low-dose rabbits (one GENTEN and three MINBEN) were fielded with an identical number of intermediate-dose rabbits.

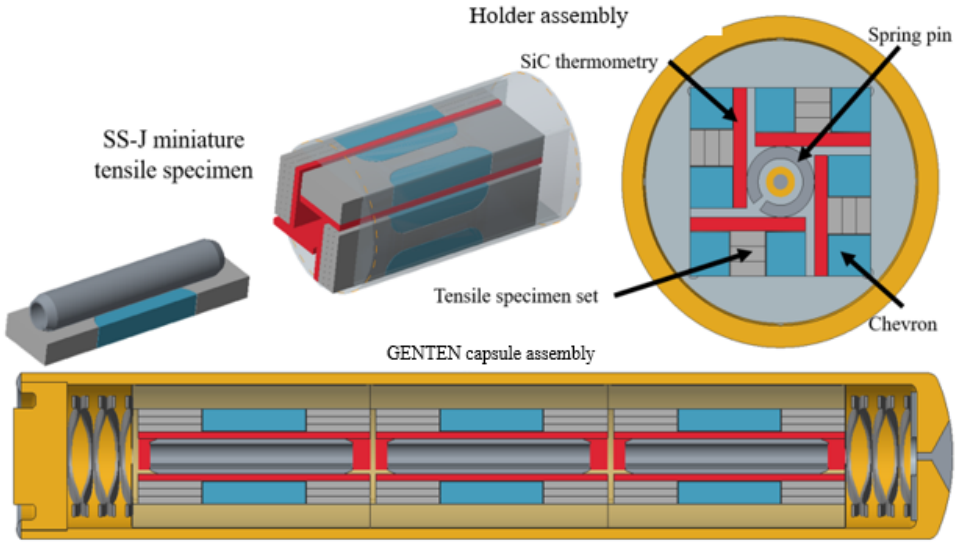

Figure 5. GENTEN capsule design [32].

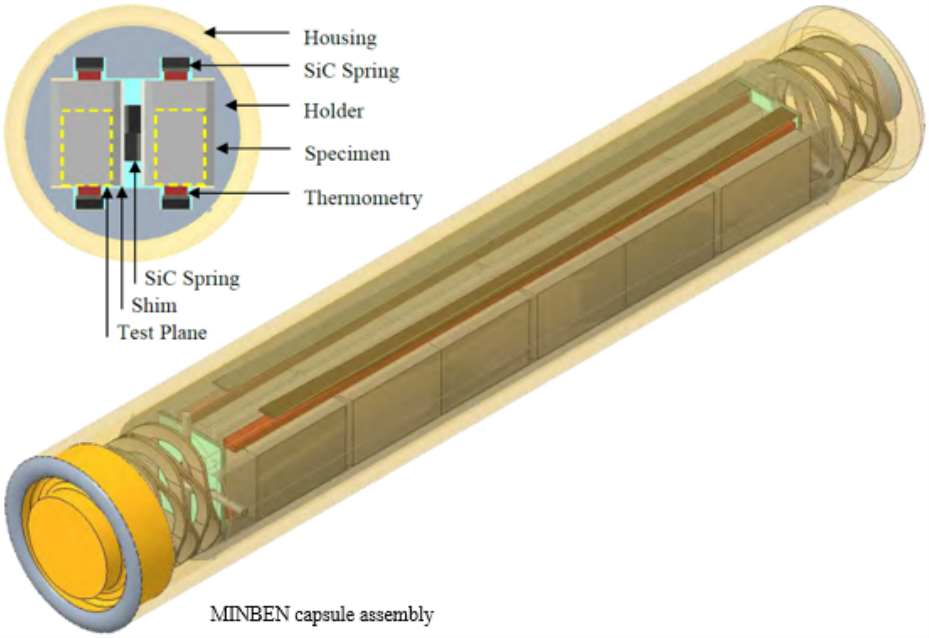

Figure 6. MINBEN capsule design [33].

To date, room-temperature post-irradiation mechanical testing has been performed on four of the six total irradiated rabbits listed in Table 2. For each of these four rabbits, passive SiC thermometry measurements were performed via dilatometry [34, 35] to evaluate the experimentally measured temperature during the irradiation, and it was found that the measured temperature generally was in good agreement with the target irradiation temperature in all cases but the 2 dpa tensile rabbit (AFT-1). It is suspected that the helium fill gas for this rabbit was contaminated during capsule welding, resulting in the capsule's average irradiation temperature greatly exceeding the target value. Since this capsule's temperature was much higher than the temperature regime relevant to irradiation hardening/embrittlement, the mechanical property data for specimens within that rabbit are omitted from the current discussion. The data from the 2 dpa fracture rabbits, as well as the tensile data from the 8 dpa rabbit, are included in the current discussion.

Table 2. AFT/AFF Capsule Design Targets vs. Actual Measured Irradiation Temperatures

Capsule	Estimated Dose [dpa]	Target specimen temp. (°C)	Experimental average specimen temp. (°C)
AFF-1	2	315	331 ± 13
AFF-2	2	315	295 ± 13
AFT-1	2	315	422 ± 35
AFT-2	8	315	278 ± 7

2.2.2 Additive Manufacturing, Oxide Dispersion Strengthened Alloys and Wrought Steels (AMOW)

The Additive Manufacturing, Oxide Dispersion Strengthened Alloys and Wrought Steels (AMOW) campaign was fielded in 2018 as a forward-looking irradiation with target irradiation doses ranging from 8 dpa to 75 dpa. The full report on the AMOW irradiation can be found elsewhere [18], and many of the materials are relevant to work conducted in the ATF and metal-fuels research areas. With respect to the FeCrAl irradiation hardening and embrittlement question, of the 9 different materials irradiated in the AMOW campaign, three of the materials were C26M-HR, C26M-WR, and the FeCrAl-ODS variant 106ZY10C.

Of the target irradiation temperatures included within the AMOW campaign (300, 385, and 525°C), only the 300°C rabbits are relevant for the current discussion, corresponding to the 3 rabbits listed in Table 3 out of the 11 total. For these three rabbits, the measured irradiation temperature was reasonably within agreement with the target temperature range. Note that the highest dpa achieved in this irradiation was about 50 dpa, which is multiple times higher than that expected for FeCrAl cladding within a conventional LWR. However, some SMR designs are considering operational conditions that would result in higher doses to fuel cladding, so the ability of the High Flux Isotope Reactor (HFIR) to accurately hit target temperatures after irradiation times approaching 6 years is important to note for future LT-ATF research.

Table 3. AMOW Capsule Design Targets vs. Actual Measured Irradiation Temperatures

Capsule	Estimated Dose [dpa]	target specimen temp. (°C)	Experimental average specimen temp. (°C)
AMOW01	8	300	324 ± 16
AMOW02	16	300	340 ± 32
AMOW03	50	300	331 ± 25

2.2.3 Ion irradiation: proof-of-principle irradiation to demonstrate hardening resistance of advanced alloys

The aforementioned AMOW campaign took years to generate irradiation hardening data as a function of alloy processing and/or composition. With current efforts to accelerate the deployment of new concepts, smart utilization of accelerated irradiation methodologies may enable faster material development and testing. Although ion irradiation may not entirely recreate the microstructures and property changes of neutron-irradiated materials, many of the same mechanisms that govern these changes are still at play and can still help predict material performance. In addition to greatly accelerated irradiation time and the ease of material handling, ion irradiation experiments also have access to a much greater degree of experimental controls. Most notably, temperature can be consistently monitored and controlled, which can help better isolate the effects of material-dependent parameters.

As a proof-of-principle experiment, excess C26M-HR and 106ZY-10C alloys from SSJ-2 sample machining were simultaneously irradiated with heavy ions at the Tennessee Ion Beam Materials Laboratory located at the University of Tennessee, Knoxville. Samples were polished to a colloidal silica (0.02 μm) surface finish and were removed from their metallography mounts. Then, the irradiation used 10 MeV Cu^{3+} ions to irradiate a section of both materials to a target mid-range dose of 10 dpa at a temperature of 300°C, confirmed using a thermocouple reading on a nearby dummy specimen. This treatment resulted in a peak damage region dose of 30 dpa and a total ion range of 2.2 μm, as calculated using SRIM-2013 (Kinchin-Pease mode, 40 eV displacement energy), for both materials. The corresponding damage and implanted ion profiles are shown in Figure 7. Temperature was controlled using a K-type thermocouple welded to a dummy sample with a very similar composition to that of C26M-HR (Fe-12Cr-6Al-2Mo-0.14Y) located directly adjacent to the samples of interest and within the irradiated region to control for beam heating effects. The thermal history of the samples during irradiation is plotted in Figure 8, which shows good temperature stability. The beam current was limited such that the dose rate in the mid-range region was 2.7×10^{-4} dpa/s. Temperature was intentionally dropped during brief beam pauses to limit any thermal annealing effects.

The mechanical properties of the ion irradiated samples were probed via nanoindentation using a KLA Nano Indenter G200X. A diamond Berkovich tip with a 1000 mN actuator was used to measure the sample modulus and hardness as a function of depth using the continuous stiffness measurement technique. The target maximum indentation depth was set to 1000 nm for each of the sample tests. The tip's area function and the load frame stiffness were calibrated using data collected from 25 indents on fused silica to a maximum depth of 2000 nm prior to sample indentation, and the lack of tip degradation during testing was confirmed by an additional 25 indents on fused silica after the completion of the sample indents. The C26M-HR sample received 30 indents in the irradiated region of the sample as well as an additional 30 indents in an unirradiated section of the sample; this latter region was outside of the ion beam area but was exposed to the same thermal history. Similarly, the 106ZY-10C sample received 118 indents in the irradiated region and another 118 indents in the unirradiated region. The larger number of indents performed on the 106ZY-10C sample was necessary to account for greater variability observed in preliminary nanoindentation tests of 106ZY-10C arising from its more complex microstructure.

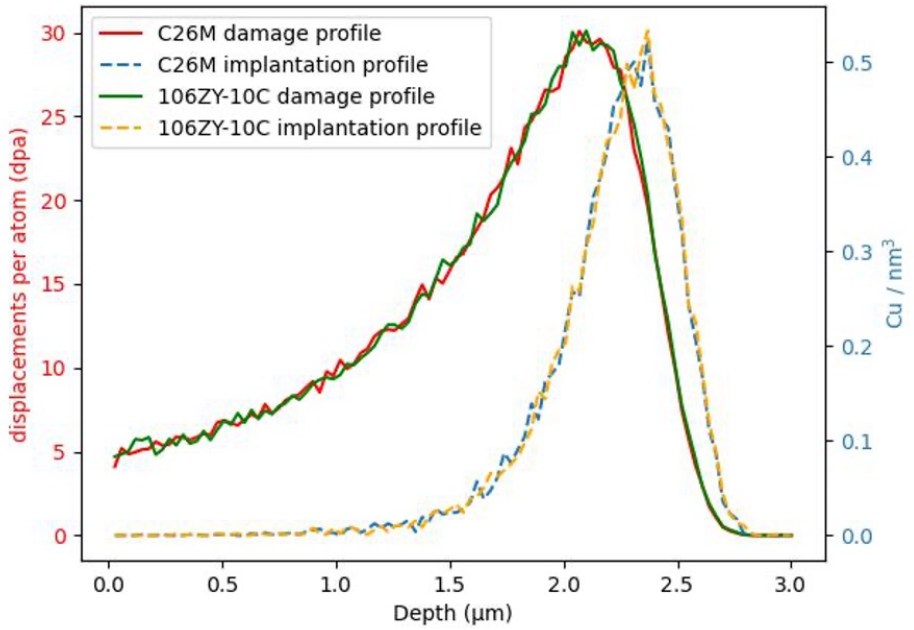

Figure 7. Cumulative dose and implanted ion concentration versus depth for C26M-HR and 106ZY-10C from 10 MeV Cu ions.

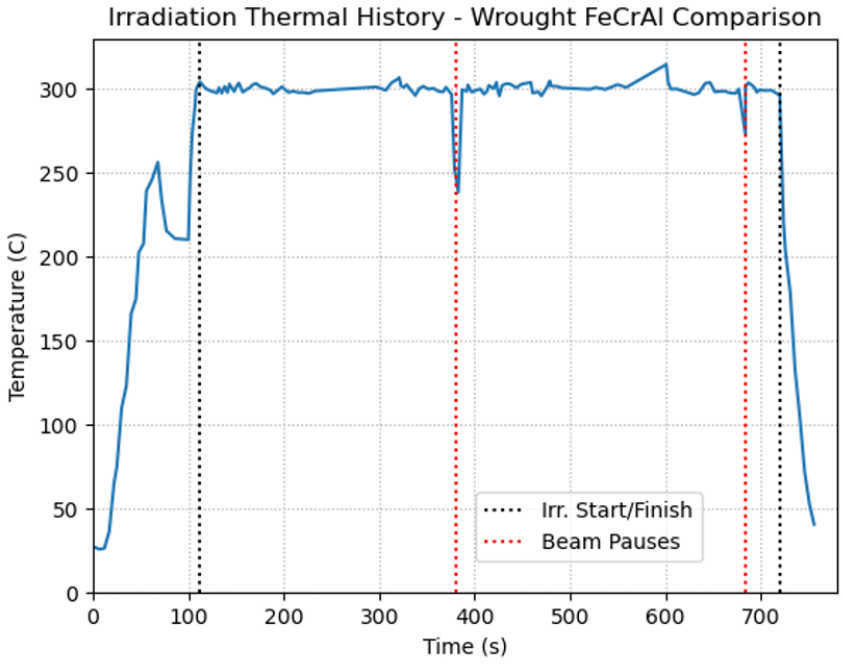

Figure 8. Thermal history of C26M-HR and 106ZY-10C during ion irradiation. **POST IRRADIATION MECHANICAL TESTING**

2.3.1 Tensile Testing of SSJ-2 Contents of AFC FeCrAl Tension Rabbit Capsule

Before each SSJ-2 specimen was placed in its corresponding rabbit, the 15C26M-HR and 106ZY-10C gauges were measured using a micrometer to confirm that they matched the pre-irradiation metrology measurements following standard quality assurance procedures. Once confirmed, these pre-irradiation measurements were used to convert raw load/displacement data into engineering stress/strain curves post-testing. After analyzing the thermometry in each tensile rabbit, the empirical temperature of irradiation was determined for the SSJ-2 contents.

Tensile testing for the FeCrAl and AFA SSJ-2 specimens was conducted with an Instron MTS 5967 mechanical tester equipped with a 5 kN rated load cell housed within the ORNL Irradiated Materials Examination and Testing (IMET) facility. SSJ-2 specimens were visually identified by the engraved cans in which they were isolated , as well as the laser engravings present on each specimen. The markings were confirmed via a remote Celestron camera present inside the hot cell. Images taken of the specimens to verify identification served the dual purpose of assessing their condition prior to placement in the fixture and providing a point of reference when documenting their post-testing integrity. The fixturing is outfitted with backstop inserts that prevent either half of a specimen from falling out after failure, which kept specimen recovery and visual comparisons consistent across the testing matrix. All tensile data presented in this work were collected at room temperature using a crosshead-displacement–controlled strain rate of 10^{-3} s^{-1}.

2.3.2 Fracture Specimen Precracking

Prior to irradiation, the miniature bend-bar specimens (MBS-1) were fatigue precracked as part of specimen preparation. This step is necessary because it ensures the maximum possible stress concentration develops during testing and therefore provides an accurate reflection of the real-world physical damage that these materials will experience during service. It was also necessary to perform this step prior to irradiation because although post-irradiation precracking is possible, it is exceedingly difficult to induce compared to pre-irradiation precracking.

Fatigue precracking was conducted in a load-controlled tension-tension mode. The MBS-1 specimen was inserted notch-down into a fixture similar to the one in Figure 9; the support span is 13 mm. The fixture was then installed in one of two TestResources servo-electric mechanical test frames. Fatigue loading was carried out at a frequency of 15 Hz ranging from a minimum load of 50 N to a variable maximum load, with high-ductility materials such as the AFAs being more tolerant of a greater maximum load and low-ductility materials such as FeCrAl alloys requiring a lower maximum load to ensure specimen survival during precracking. For the materials characterized in this report, the maximum load of the AFAs during precracking was 675–700 N, whereas the maximum load was 450 N for C26M4 and these steps were conducted at room temperature. For C26M-0Y, precracking at room temperature was found to be exceptionally difficult without destroying the specimens: in the interest of conserving the small amount of material available, this material was precracked with a maximum load of 675 N at 200°C.

The desired total precrack length (fatigue crack + starter notch) is approximately half the specimen thickness. Due to the exceptionally small specimen size employed, direct crack growth

measurements via notch mouth clip gauge or direct current potential drop (DCPD) were not possible. Instead, a gauge-free method was employed to determine crack growth. After precracking was initiated, the specimen was allowed to "break-in" for 3,000–10,000 cycles, whereby the cyclic loading early in the step resulted in plastic deformation saturation at the contact points between the specimen and fixture; this was necessary to ensure that any changes in specimen compliance were a result of crack growth only. At this point, the peak displacement value was noted and the test system was then programmed to terminate the precracking step once the peak displacement had increased beyond a particular threshold.

The requisite change in peak displacement is dependent on the mechanical and elastic properties of the material in question, as well as the peak load, specimen geometry, and loading configuration. For materials loaded to high (675-700 N) maximum loads, a change in peak displacement of approximately 20 μm was necessary to achieve the approximate desired precrack length, whereas for the brittle C26M4 the change in peak displacement was approximately 8 μm; this low displacement change was necessary to avoid specimen failure during precracking. A final cycle count of 30,000-50,000 cycles is generally desired in the interest of time, but for low-ductility materials hundreds of thousands of cycles are often necessary to ensure both adequate crack growth and specimen integrity. Once the requisite change in peak displacement had been achieved, the maximum load was reduced such that the load amplitude was half that of the initial precracking step. The specimen was then cyclically loaded for another 10,000 cycles at this reduced amplitude to sharpen the fatigue crack tip, thereby ensuring a high stress concentration upon testing. Upon completion of this secondary step, the specimen was removed from the fixture and stored for later testing or irradiation.

Figure 9. MBS-1 three-point bend fixturing.

2.3.3 Fracture Toughness Testing and Evaluation

Fracture testing was performed by reloading the precracked specimen into the fracture fixture and installing the fixture into the frame, similar to the precracking step. For 300°C tests, a 20 N preload was applied to ensure tension was maintained during thermal expansion of the load train. Specimen temperature was monitored directly via a thermocouple inserted into a port machined into the back of the fixture near the crack. Once the temperature was within ±5°C of the nominal test temperature, the fixture was allowed a 5-minute soak time to ensure thermal stability and proper temperature range in the vicinity of the specimen crack. After the soaking period, the specimen was loaded in a displacement-controlled tension-mode three-point bend at 5 µm/s. The test was terminated either when total specimen failure occurred, as was the case for the FeCrAl materials tested at room temperature, or, for ductile fracture behavior, when the load had dropped to approximately half the peak of the load-displacement curve, or when an excessive (~4.5-5 mm) displacement had occurred.

In addition to load-displacement data, fracture length data are required for a complete fracture data set. First, for specimens that demonstrated ductile fracture, these specimens were heated in air to approximately 400-450°C or until a noticeable change in fracture surface color occurred; this step was not necessary for specimens that demonstrated unstable fracture. This color change marks the final crack length. Following this heat tinting step, the specimens were then fully broken by hand, as was the case for the unirradiated specimens, or by reinsertion into the fracture fixture and loading until total failure, as was the case for the irradiated specimens. The fracture surfaces were then imaged, as shown in Figure 10.

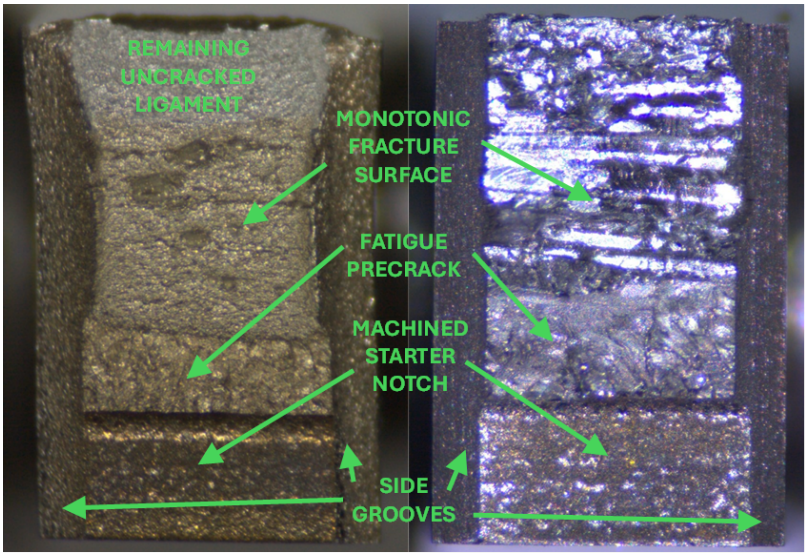

Figure 10. (Left) fracture surface image of ductile AFA specimen that demonstrated stable fracture and (right) fracture surface image of brittle FeCrAl specimen that exhibited unstable fracture. Note that the final crack length of the ductile specimen has been marked via heat tinting. Also note the difference in fracture surface texture, with the ductile specimen displaying a fine, dimpled fracture surface texture, whereas the brittle specimen displays a coarse, faceted texture. Fracture lengths were measured in accordance with ASTM E1820-18 [36], with nine evenly spaced points at the initial and final crack fronts

measured from the specimen bottom; in the case of unstable failure, only the initial crack length measurement is necessary. Image distances were measured in pixels, then converted to length using the undeformed specimen bottom as a reference scale. The points measured at the specimen side grooves were weighted by 0.5, then the initial and final crack length measurement sets were averaged by a factor of 8. For unirradiated specimens both surfaces were imaged and measured, and the values between the two were averaged. For irradiated specimens, only one fracture surface per specimen was imaged given the difficulty in positioning and imaging specimens in a hot cell, though this is still sufficient.

With the load-displacement and crack length data obtained, fracture toughness data could then be calculated. For fracture specimens that display no plastic deformation whatsoever, calculating the critical stress intensity factor K is simple [36]:

$$K = \frac{PS}{(BB_N)^{0.5}W^{1.5}} 3\left(\frac{a}{W}\right)^{0.5}\left(1.99 - \frac{a}{W}\left(1-\frac{a}{W}\right)\right)\left(2.15 - 3.93\frac{a}{W} + 2.7\left(\frac{a}{W}\right)^2\right)\left(2\left(1+2\frac{a}{W}\right)\left(1-\frac{a}{W}\right)^{1.5}\right) \quad (1)$$

where P is the load at failure, S is the span of the three-point bend, B is the specimen width, B_N is the width at the side grooves, W is the specimen thickness, and a is the crack length.

For specimens that demonstrate any degree of plastic deformation, J-R fracture data must be calculated. Physically, J-R data represents the amount of energy necessary for the generation of new fracture surface, with high toughness materials demonstrating high J values and low toughness materials demonstrating low values. For this work, a modified version of the curve normalization method as outlined in [36] was employed. The curve normalization method is the only practicable method available given the exceptionally small specimen size, high ductility of certain materials such as unirradiated AFA or elevated temperature FeCrAl, and the difficulty, if not impossibility, of other methods at elevated temperatures or post-irradiation.

The curve normalization method allows for direct extraction of mechanical energy dissipation (i.e. toughness) by factoring out the compliance of the load train as well as the elastic compliance of the specimen, which changes with changing crack length. This methodology is analogous to uniaxial tensile testing where strain data are derived by extracting the elastic load train compliance from the raw load-displacement data; while not as precise as direct measurements, for the vast majority of applications it is acceptable. As mentioned previously, the method was modified relative to [36] in order to accommodate the exceptionally small specimen geometry and high ductility for materials that displayed it; it was found early in the testing campaign that direct application of the method often leads to nonsensical results. The modifications are (1) crack length in the blunting region is assumed constant during primary calculations, (2) the remaining bearing ligament (W-a) is assumed to be proportional to the remaining unshed load in the crack propagation regime, (3) the relationship between normalized displacement and normalized load is assumed to be linear in the crack propagation regime, and (4) the flow stress is defined as the average of the yield and *true* ultimate tensile strength rather than the *engineering* ultimate tensile strength. By assuming constant crack length in the blunting regime as the data are initially calculated, the crack extension values are corrected post-calculation to compensate for plastic deformation during blunting:

$$\Delta a_i = \Delta a_{i,0} + \frac{J_i}{2\sigma_{\text{flow}}} \tag{2}$$

where Δa_i is the corrected crack extension for point i, $\Delta a_{i,0}$ is the interim crack extension value prior to compensation, J_i is the corresponding J value, and σ_{flow} is the flow stress. With the J_i and Δa_i sets calculated, the J-R curve can then be constructed, as shown in Figure 11.

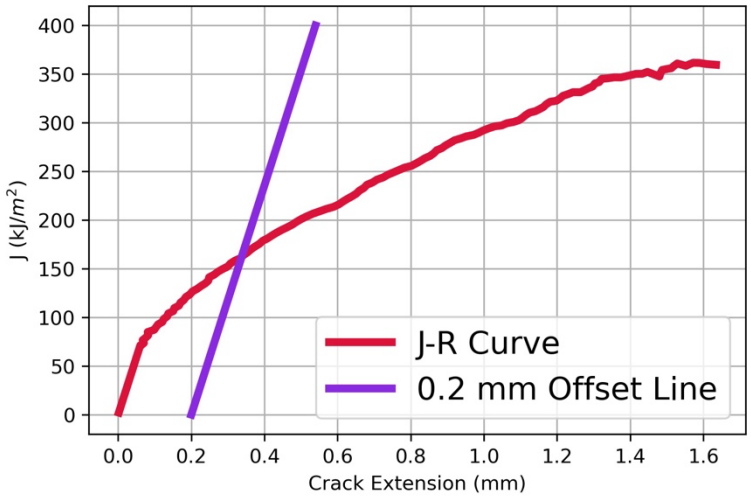

Figure 11. J-R curve with 0.2 mm offset line.

The J-R curve in Figure 11 is displayed along with the 0.2 mm offset line, a line with the same slope as the blunting region of the J-R curve and an x-intercept of 0.2 mm. Unlike brittle materials, ductile materials do not have a critical stress intensity K_{IC} which results in immediate failure. Therefore, in order to create a means of comparison between brittle and ductile materials, as well as to simplify comparison between varying materials and conditions, an interim stress intensity K_Q is established. Though the derivation of this value can vary depending on the application, it is common practice to utilize the K value derived at the 0.2 mm offset as the reported value [37], analogous to how yield stress is often reported as the stress value at 0.2% plastic strain. The $J_{0.2mm}$ value is determined by the intersection of the J-R curve and offset line. The $K_{0.2mm}$ value is then calculated as:

$$K_{0.2\text{mm}} = \sqrt{\frac{EJ_{0.2\text{mm}}}{1-\nu^2}} \tag{3}$$

where E is the elastic modulus and ν is Poisson's ratio. Equation (3) assumes plane-strain conditions are satisfied. In actuality, for highly ductile materials at small geometries, plane-strain conditions will not be satisfied, but this is generally understood amongst nuclear-oriented fracture mechanists, and it is common practice to report interim K_Q values as per Equation 3 regardless. Because plane-strain conditions are not satisfied for the more ductile materials, it is not recommended that the derived toughness data be used as an engineering basis, particularly for large, bulky geometries. As J-R fracture toughness is a *structural* property rather than a

material property, it is scale-dependent, with smaller geometries leading to overestimates of toughness relative to larger geometries. However, data derived from the MBS-1 geometry is useful for screening purposes as well as to evaluate how the relative fracture behavior of a material changes with changes in condition (temperature, irradiation dose, etc.). In the case of brittle failure, such data may be used more reliably as a design base. Generally, the plane-strain condition is considered satisfied when the specimen thickness is greater than ten times the radius of the plastic zone around the crack tip. As there is little to no plastic zone surrounding the crack tip in the case of brittle failure, the plane-strain condition is therefore satisfied, and the data may be viable as an engineering basis.

3. RESULTS AND DISCUSSION

3.1 EFFECT OF COMPOSITION AND PROCESSING HISTORY

The first hypothesis that requires evaluation concerns the extent to which minor changes in alloying or processing can affect the irradiation hardening response of FeCrAl alloys. In fact, the margin of error in conventional neutron irradiation experiments has created some ambiguity in prior irradiations of compositionally varying FeCrAl alloys. In the initial series of FeCrAl irradiations (within the FCAY campaign), it was found that some retained ductility existed in simplified compositions of low-Cr (12 wt%) FeCrAl variants, while higher-Cr variants (18 wt%) failed in the elastic region of the tensile test. This experiment correctly identified Fe-Cr phase separation as a major issue exacerbating the irradiation hardening and embrittlement problem [4]. However, the high-dose condition used as an example for retained ductility had a measured irradiation temperature of 341°C, which is arguably above the relevant irradiation temperature range for LWRs. The second major irradiation campaign for FeCrAl alloys (FCAT) showed essentially no retained ductility even for the low-Cr FeCrAl alloys with nominal compositions of Fe-(10-13)Cr-(6-7)Al-2Mo wt%, and all of these samples were tested at a measured irradiation temperature much closer to those of prototypic conditions (~280°C) [7]. With the 60–100°C variance of irradiation temperatures between the FCAY and FCAT irradiations, the irradiation campaigns in this work intentionally changed only the minor alloying compositions to clarify the effect of elements like Mo and Y on the irradiation hardening behavior in the same irradiation capsule.

To assess the effect of composition, the conventional C26M alloy (C26M4) was compared to C26M-0Y (Y-free) and B126N (Y-free and Mo-free) (Figure 12) following irradiation in HFIR to 8 dpa at a measured irradiation temperature of 278°C. The blue curves in the figure represent the unirradiated data, while the black curves represent room temperature tensile tests of the irradiated specimens. Before irradiation, the B126N material had the highest ductility among the three Fe-12Cr-6Al plates, with the lowest corresponding yield strength due to its lack of solid solution strengthening from Mo in the other two alloys. There were load drops observed in the C26M4 alloy, which are consistent with microcracking over the course of the tensile test. This indicates that this specific heat of C26M may not be the most representative heat to use for a comparison.

After irradiation, all three heats, regardless of prior ductility, suffered failure in the elastic region of tensile deformation characterized by a linear rise to a maximum load, followed by an

instantaneous drop in load as the sample fractured. Due to this brittle behavior, it is not correct to call this maximum stress either the yield stress (YS) or ultimate tensile stress (UTS) because it is likely that at least a subset of these three specimens failed stochastically before the YS was even reached. These results indicate that simply removing the intermetallic-forming elements (yttrium) or the solid-solution strengthening elements (Mo) from FeCrAl alloys does not significantly alter the mechanism by which these BCC alloys embrittle following low-temperature neutron irradiation.

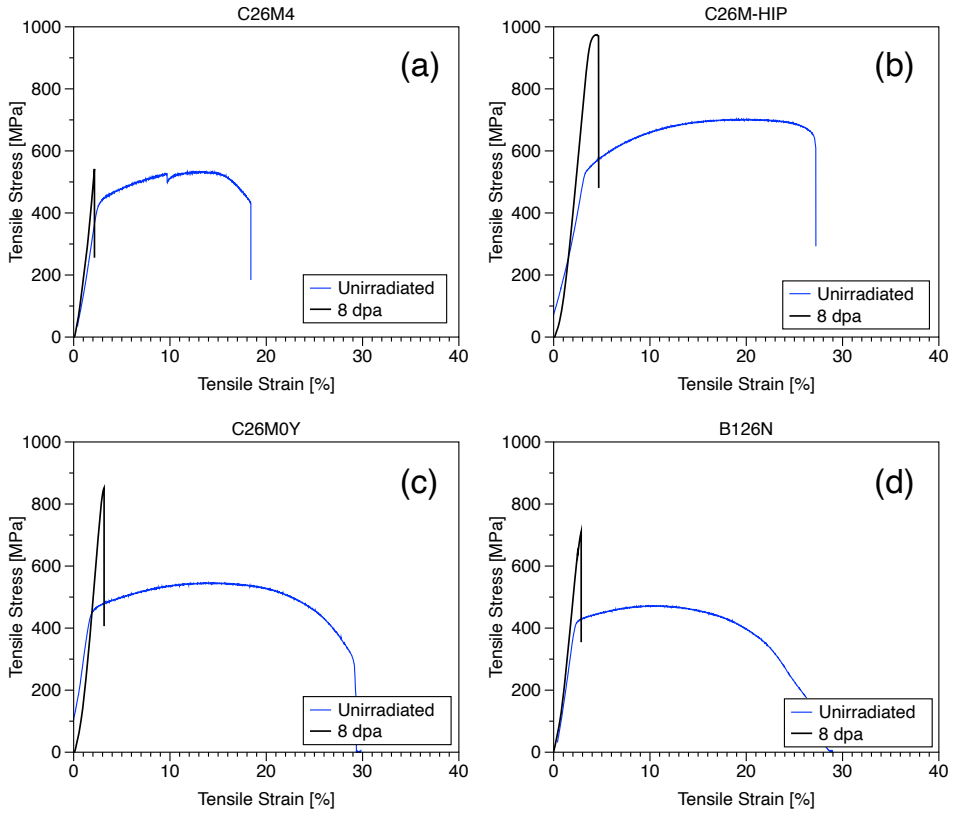

Figure 12. Unirradiated and HFIR-irradiated room-temperature engineering stress-strain curves for (a) C26M4, (b) C26M-HIP, (c) C26M-0Y, and (d) B126N. Irradiation conditions for all samples are 8 dpa at 278°C. In addition to alloy composition, a secondary hypothesis that is highly relevant to forward-looking FeCrAl development efforts is the effect to which alternative processing methods can change the irradiation hardening behavior of this alloy system. In the same Figure 12, a comparison can be made between the alloy C26M-0Y and the C26M-HIP sample. Both alloys have the same C26M nominal composition, without the trace amounts of yttrium. Yttrium is well known to be important for extending the high-temperature threshold for oxidation resistance in FeCrAl alloys due to the reactive element effect [38], but yttrium is also insoluble in Fe and precipitates out into brittle intermetallic phases on grain boundaries that amorphize under irradiation [19]. In the current work, the C26M-HIP material was produced without yttrium primarily due to the difficulty of gas atomizing powder with uniformly distributed yttrium for the same reason. Both of the two alloys have unirradiated ductility exceeding 25% with considerable work-hardening capacity, but the HIP'd alloy has much higher initial strength due to its finer grain size and larger Hall-Petch strengthening contribution.

Following irradiation, the C26M-HIP material also loses most of its ductility at 8 dpa, but it does appear to pass the yield point, with a measured YS of 870 MPa, a UTS of 975 MPa, a uniform elongation (UE) of 0.75%, and a total elongation (TE) of 0.91%. Less than 1% plastic strain to failure is still not an optimistic outcome, but having some measurable ductility and the ability to accommodate some plastic strain is notably better than the other three wrought variants that failed at or before the YS. From these results, it is true that the material subject to HIP performs better than wrought variants at these irradiation conditions, but it does so only marginally.

3.1.1 Comparing BCC FeCrAl and FCC AFAs

Within the same AFT-2 rabbit were three AFAs designed for potential use as ATF fuel cladding for direct comparison with the BCC FeCrAl alloys. As stated previously, AFAs are a compositionally complex class of materials and the specific major and minor alloying elements can be tuned to produce specific properties of interest. For the first iteration of potential AFAs for ATF cladding, the alloys were designed with the intent of (1) maximizing the stability of the alumina scale formed during high-temperature steam oxidation, and (2) providing enhanced high-temperature strength. One method to accomplish this task is to leverage highly reactive elements like Nb that help stabilize the oxide scale at high temperature while also forming strengthening carbides throughout the microstructure. However, it is unclear if the significant additions of Nb (up to 2.5 wt%) will result in unacceptable levels of embrittlement following irradiation, especially when compounded with other expected degradation mechanisms.

Figure 13 presents the unirradiated and irradiated tensile curves of the AFC AFA series of alloys with 0.6 wt% Nb (AA06), 1.0 wt% Nb (AA07), and 2.5 wt% Nb (AA09). In the unirradiated state, all three alloys have a low yield strength (~300 MPa), which is about 60% of the PM-HIP version of C26M at room temperature. With the high stresses that are expected to be imparted on the FeCrAl cladding in the event of pellet-cladding mechanical interaction [39, 40], the lower initial YS of the AFAs may be beneficial in some scenarios, such as reactivity-initiated accidents.

Following irradiation to 8 dpa at 278°C, the AFAs exhibit significant hardening, increasing in yield strength to over 900 MPa for the lower-Nb content alloys and to above 1100 MPa for the higher Nb-containing alloy. This increase in hardness is also associated with a decrease in total elongation to between 5-6% consistently across all three alloys, with negligible UEs ranging from 0.25% to 0.63%. This immediate onset into strain localization is common for stainless steels and Zr-based alloys at low irradiation temperatures [41], and the loss of ductility measured in this work is similar to other irradiations of austenitic stainless steel available in the literature [42]. Compared to the BCC FeCrAl alloys, these materials have much higher retained ductility and also exhibit high strengths after irradiation, which is a potential benefit if other potential issues are resolved for this alloy concept.

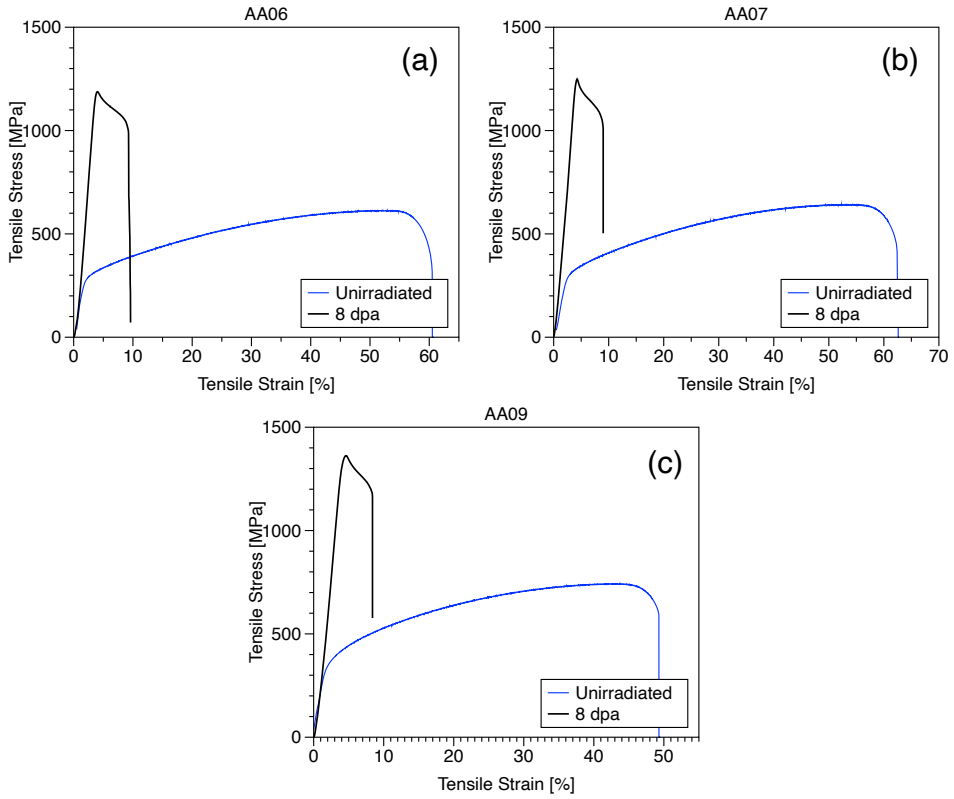

Figure 13. Unirradiated and HFIR-irradiated room-temperature engineering stress-strain curves for (a) AA06, (b) AA07, and (c) AA09. Irradiation conditions for all samples are 8 dpa at 278°C.

The retained ductility of the AFAs is only one component of the feasibility evaluation, with the other component being fracture toughness. Many authors erroneously conflate irradiation hardening with embrittlement, whereby the claim of retained ductility is also used to argue that the alloy has not embrittled. This is an erroneous assumption, as this latter metric requires specific measurements, whether it be from Charpy impact or fracture toughness measurements, to establish the resistance of crack propagation before and after irradiation. The AFAs investigated as potential ATF candidates have high Fe, Cr, Ni, and Al contents, with minor additions of elements like Mn, Nb, Mo, Si, and C. Previous thermodynamic assessments and metallurgical characterization have confirmed that in the as-processed state, there are precipitates such as B2 (NiAl) and carbides (Nb-rich) in the unirradiated materials. In addition, other phases that are predicted to form include G-phase, Laves phase (Fe_2Nb), and Cr-rich alpha-prime. In addition to the stacking fault tetrahedra and loop populations, these secondary phases may all coexist in some volume fraction resulting in the prior large strength changes measured after irradiation, which would require further characterization to confirm. Not only this, but the large Ni content is expected to produce approximately 700 appm He over the course of the 8 dpa HFIR irradiation, which may significantly embrittle the cladding candidate.

To address this issue, several miniature bend bars were subjected to room temperature fracture toughness measurements before and after irradiation through the AFF campaign. In the prior literature on design criteria for materials for fission/fusion energy, a fracture toughness threshold of ~30 MPa$\sqrt{m}$ has been used to establish the lower temperature limit for material use [43]. Using these criteria, we can then evaluate which materials pass this threshold in the unirradiated

and irradiated cases at room temperature by evaluating the individual measurements of fracture toughness at 0 dpa (unirradiated condition) and 2 dpa (irradiated condition); these results are compared in Figure 14.

For the unirradiated BCC FeCrAl alloys, room temperature fracture toughness is already near or below the disqualification threshold, while the fracture toughness measured at operational temperature is much higher. This is already known for this class of alloys, since it has been previously shown that the ductile to brittle transition temperature is near 100°C for low-Cr FeCrAl alloys with large Al-contents (~6% wt%) [2]. As such, these unirradiated fracture toughness measurements are analogous to historical Charpy impact measurements that would establish the upper shelf and lower shelf energies absorbed to propagate cracks through materials. Since the room-temperature fracture toughness measurements are so low even in the unirradiated condition, it is unsurprising then that there is little room for the fracture toughness to decrease even further post-irradiation for the wrought FeCrAl materials.

The AFA materials show a much different behavior at room temperature and following irradiation. For instance, in the unirradiated condition, the fracture toughness at room temperature and when tested at 300°C is quite high, although with increasing Nb content Figure 14 shows that the unirradiated fracture toughness does monotonically decrease from 533 MPa√m (with 0.6 wt% Nb) down to 221 MPa√m (with 2.5 wt% Nb). This higher Nb content, therefore, provides a lower allowable margin for fracture toughness deterioration. Following irradiation to 2 dpa, the room temperature fracture toughness of all three alloys decreases to similar values ranging between 122-225 MPa√m, and it would be expected that these values would continue to decrease with increasing irradiation dose up to ~8 dpa [2], but that data has not yet been collected to evaluate whether this fracture toughness criterion is met. It is therefore still too early

to establish whether AFAs are suitable as an LT-ATF candidate.

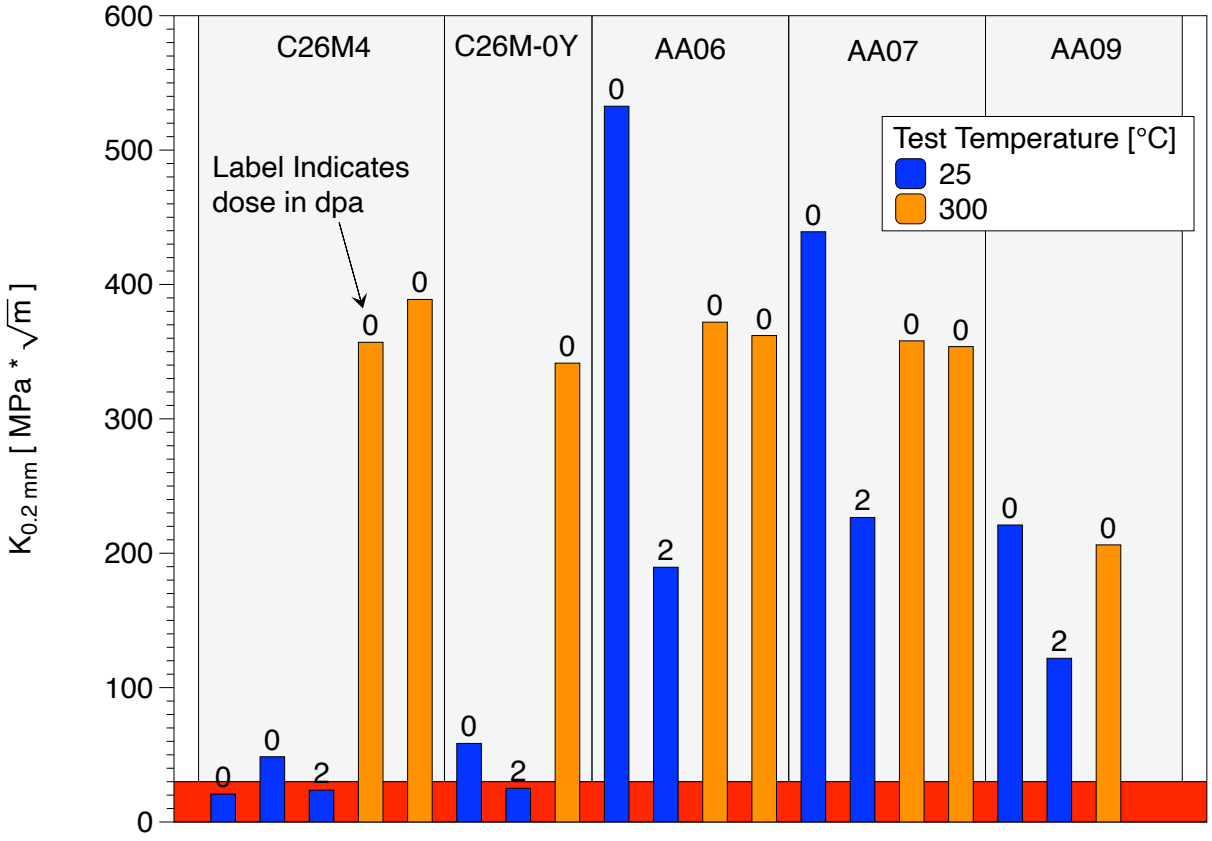

Figure 14. Pre- and Post-irradiation fracture toughness measured for two FeCrAl alloys and three AFAs tested at RT (blue) and at 300°C (orange).

3.1.2 Comparing Wrought and ODS FeCrAl (at even higher doses)

In previous work, it has been demonstrated even in the earliest low-Cr FeCrAl irradiation campaigns [44] that FeCrAl-ODS materials have the potential to outperform wrought variants in terms of irradiation-induced mechanical property degradation. Follow-on research has since demonstrated that the high sink strength of the FeCrAl-ODS material [45], combined with the destabilization of Cr-rich alpha-prime [3], results in lower densities of Cr-rich precipitates in FeCrAl-ODS vs. its wrought counterparts [26]. However, research to date has not confirmed whether the initial results presented in this prior literature on low-dose neutron irradiation conditions extends to prototypic doses representative of end-of-life conditions for the alloy system. Within the AMOW irradiation campaign, the hot-rolled and warm-rolled C26M were compared directly with alloy 106ZY10C to doses as high as 50 dpa with a target irradiation temperature of 300°C. The actual irradiation temperatures measured were slightly higher and are listed in Table 3, but they are all within normal errors associated with neutron irradiation campaigns. In addition, even with slight variations in irradiation temperature across the three

dose conditions, a 1:1 comparison can still be made within each dose condition among the three materials of interest.

A comparison of the tensile curves for the two wrought FeCrAl variants and the ODS variant are provided in Figure 15. Before expanding on the post-irradiation properties, there are notable differences among the three materials even in the unirradiated state. For instance, the hot-rolled variant of C26M shows the highest level of ductility of the three materials but has a lower initial strength. This variant is more representative of a high-performance heat of wrought FeCrAl vs the prior C26M4 material shown in the prior sections of this report. When the additional warm-rolling process was conducted on the material, generating the C26M-WR variant, the material becomes work hardened to a point where the yield strength increases by almost 300 MPa. However, this increase in strength through an increase of dislocation density comes at the cost of ductility, and the C26M-WR material has essentially no work hardening capability and much lower total elongation as a result of this additional thermomechanical processing treatment. These two conditions represent ideal samples to investigate the effect of moderate and high network dislocation content on the irradiation performance of wrought FeCrAl alloys. The FeCrAl-ODS material has >1 GPa strength with approximately 20% total elongation in the as-extruded state, showing superior unirradiated performance to both wrought FeCrAl alloys.

Following irradiation, both wrought FeCrAl alloys eventually lose all ductility, but at different rates. For the more representative C26M-HR material, some retained ductility is observed after 8 dpa, and the material does yield before suffering fracture in the 16 dpa condition. However, by 50 dpa, the C26M-HR material shows no ability to accommodate plastic strain prior to sudden, presumably brittle, fracture. For the C26M-WR material, a similar trend is observed but at a faster rate, with the material losing all ductility by only 8 dpa and failing in the elastic regime in all three dose conditions. With these irradiations occurring in the 320-340°C regime, this ductility loss is expected to only be more severe at lower temperatures more representative of LWR operation.

In contrast to the rapid loss of ductility for the wrought FeCrAl alloys, the FeCrAl-ODS material demonstrates superior resistance to irradiation-induced degradation at the same conditions. Although the total ductility and the strain hardening capacity do decrease as a function of increasing dose, the material retains almost 10% total elongation even after irradiation to 50 dpa, which is over 3 times the maximum dose expected in a conventional light water reactor cladding. A comparison of the strength evolution and ductility retention of the three materials is summarized in Figure 16.

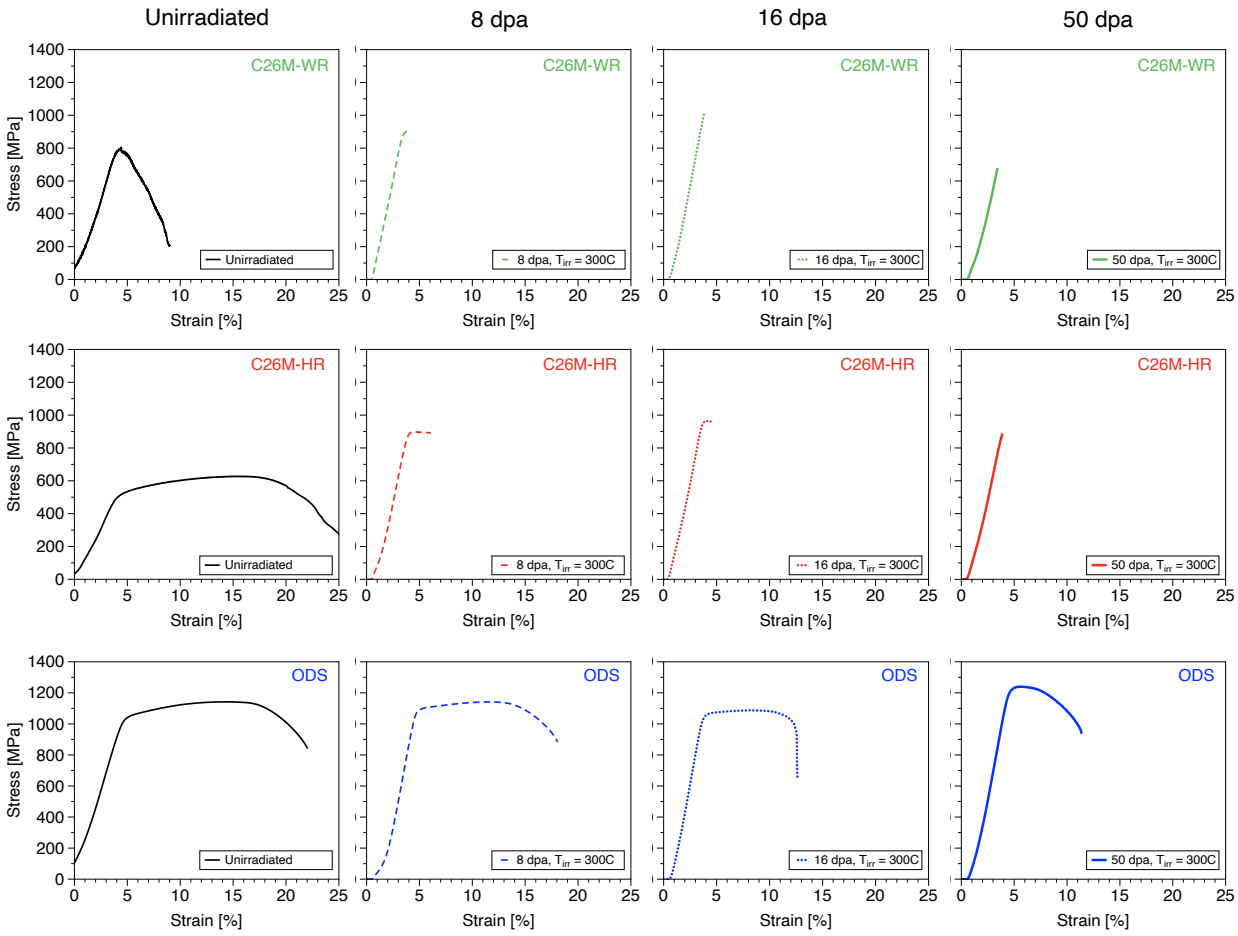

Figure 15. Unirradiated and HFIR-irradiated room-temperature engineering stress-strain curves for C26M-WR, C26M-HR, and FeCrAl-ODS material 106ZY10C to increasing doses at a target irradiation temperature of 300°C.

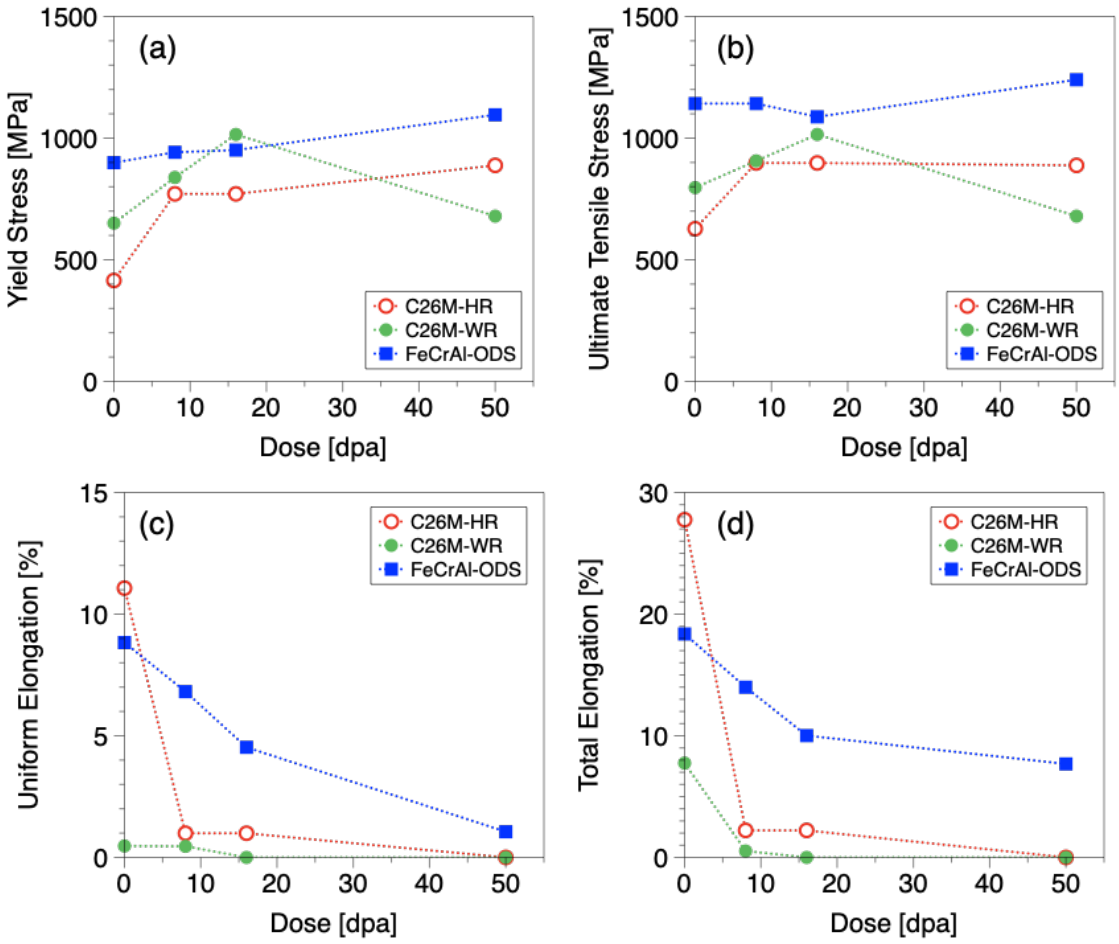

Figure 16. Evolution of (a) YS, (b) UTS, (c) UE, and (d) TE as a function of dose for FeCrAl-ODS (106ZY10C) and wrought FeCrAl materials irradiated up to 50 dpa in HFIR at a target irradiation temperature of 300°C. One test per condition is shown.

The results of this high-dose comparison give a strong argument for the continued research into FeCrAl-ODS alloys for advanced LWR LT-ATF cladding, as well as advanced irradiation-resistant materials for next-generation SMR technologies. More research is needed, however, since the evolution of an as-extruded form of ODS material is not necessarily representative of the performance of prototypic cladding. For instance, when an extruded master rod is pilgered into a final thin-walled tube geometry, the grain size is highly refined and significant residual stress remains within the thin-walled cladding. This severe work hardening could result in an as-pilgered FeCrAl-ODS material behaving in a high-strength but low-ductility manner [46], which could prove deleterious for post-irradiation performance. Conversely, performing a high-temperature recrystallization anneal may be advantageous in increasing high-temperature creep performance [24] but could decrease the effective sink strength of the material, thereby making it no longer resistant to irradiation hardening and embrittlement to the same extent. This last conjecture has yet to be proven through systematic post-irradiation investigations but is of interest to current joint research efforts within current international collaborations between the United States and Japan.

3.1.3 Irradiation hardening response of Wrought vs. ODS FeCrAl ascertained from accelerated ion irradiation

Nanoindentation data were analyzed using the Nix–Gao model [47] to account for the indentation size effect and to selectively extract mechanical property information from the thin damaged layer of ion irradiated material without substantial influence from the softer unirradiated material underneath. According to the Nix–Gao model, plotting the square of the measured hardness versus the inverse depth should yield a straight line for a homogeneous material with the slope corresponding to a characteristic indentation size effect length and the intercept corresponding to an estimated bulk equivalent hardness that would be measured from an infinitely deep indent. As shown in Figure 17, when the data from the ion irradiated materials are plotted in this manner, a slope change is apparent after a depth of approximately 350 nm, indicating the onset of influence from the deeper unirradiated material on the measured hardness. This is due to the geometrically necessary dislocations produced by the indenter tip encountering substantially less resistance to glide after passing through the steep drop off in dislocation loop density beneath the end of the ion range 2200 nm below the surface. To estimate the bulk equivalent hardness of the irradiated region alone, linear regression of the data was consequently restricted to the depth range of 200–350 nm. This excludes data deeper than the inflexion point while also discarding data from low indent depths that may have inaccuracies introduced from blunting of the indenter tip.

The data for each set of indents in the irradiated and unirradiated areas of the C26M-HR and 106ZY-10C samples were compiled together to form a set of 4 master curves. The bulk equivalent hardness estimated by linear regression of data in the 200–350 nm depth range from these 4 master curves is shown in Table 4. The C26M-HR experienced an objective increase in bulk equivalent hardness following the low temperature ion irradiation that was nearly twice as large as that of the 106ZY-10C material, although the initial unirradiated hardness of the 106ZY-10C was considerably larger than that of the C26M-HR. This behavior qualitatively matches the improved irradiation hardening resistance of the ODS 106ZY-10C over the C26M in the neutron irradiated data, illustrating how accelerated ion irradiations can be a useful tool for assessing the relative mechanical property changes of materials under irradiation. This can possibly aid in down-selecting promising candidate materials prior to lengthier neutron irradiation experiments.

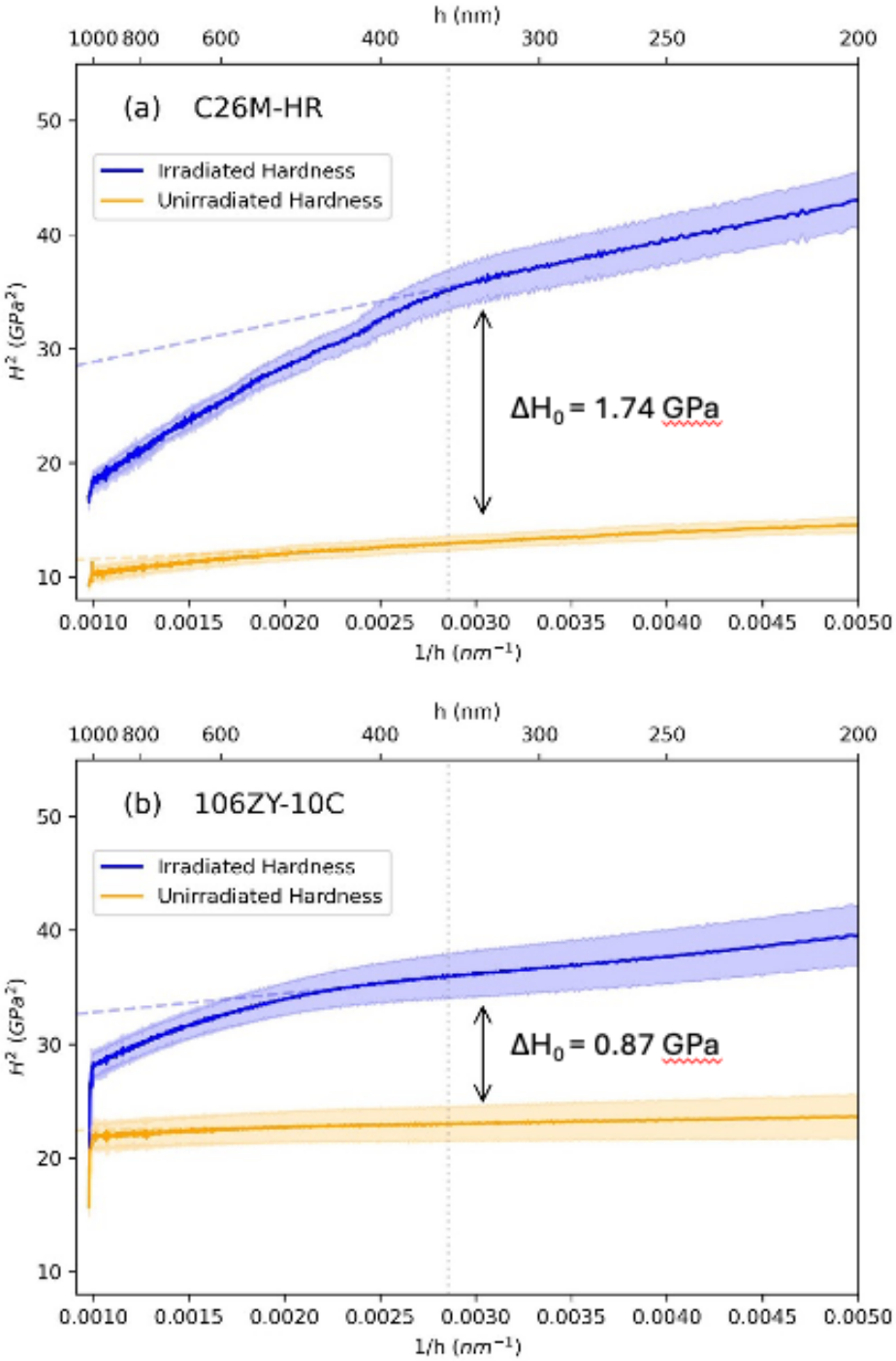

Figure 17. Nix–Gao plots of squared hardness versus inverse depth for (a) C26M-HR and (b) 106ZY-10C showing relative hardness increases and the appearance of a slope inflexion point following ion irradiation.

Table 4. Bulk equivalent hardness of ion irradiated and unirradiated regions of C26M-HR and 106ZY-10C as calculated using the Nix–Gao model with restricted depth range for fitting

Sample	Nix–Gao H_0 using 200–350 nm fit depth range (GPa / Vickers hardness units)	Relative hardness increase (GPa / Vickers hardness units)
C26M-HR Ion Irradiated 300°C	5.032 ± 0.015 GPa (476.1 ± 1.4 HV)	1.686 ± 0.023 GPa (159.5 ± 2.18 HV)
C26M-HR Unirradiated 300°C	3.346 ± 0.008 GPa (316.6 ± 0.8 HV)	
106ZY-10C Irradiated 300°C	5.581 ± 0.008 GPa (528.0 ± 0.8 HV)	0.873 ± 0.015 GPa (82.7 ± 1.4 HV)
106ZY-10C Unirradiated 300°C	4.708 ± 0.007 GPa (445.4 ± 0.7 HV)	

4. CONCLUSIONS (AND FUTURE WORK)

Oak Ridge National Laboratory recently completed post-irradiation mechanical property investigations into various permutations of alumina-forming Fe-based alloys, including both BCC (FeCrAl, FeCrAl-ODS) and FCC (AFA) variants. Multiple irradiation vehicles were fielded within the HFIR at target temperatures in the range of 300–315°C to doses in the 2–50 dpa range, and both tensile and fracture toughness properties have been collected to date on irradiated materials. From these results, the following conclusions have been ascertained.

- There is a negligible effect on minor alloying elements such as Mo and Y on the ductility-retention of alloy C26M following neutron irradiation. The wrought C26M material, when irradiated at temperatures at or below 300°C, loses all ductility by the time irradiation-induced defects saturate (~ 8 dpa).
- The use of fully recrystallized PM-HIP does have a marginal improvement on the retained post-irradiation ductility of C26M following neutron irradiation to 8 dpa, but the effect is minor, and it is yet unclear what the retained ductility of PM-HIP C26M would be at a simulated end-of-life (16 dpa) dose level.
- AFAs designed for ATF application have been initially screened in the current irradiation campaign. After a dose of 2 dpa, the AFAs easily retain suitably high fracture toughness levels ($K_{0.2mm}$ = 122-225 MPa$\sqrt{m}$). In addition, their total ductility levels following 8 dpa irradiation remain at 5–6% depending on composition, which is similar to other historical stainless steels irradiated in similar conditions. Even with these positive indicators, there remain significant questions about end-of-life tensile ductility and fracture toughness due to (1) potential radiation- enhanced precipitation of secondary phases and (2) high He-production within the microstructure as a function of increasing fluence. Finally, there has not yet been a comprehensive study on activation, corrosion, or oxidation on these materials beyond the limited screening performed prior to neutron irradiation in this effort.
- FeCrAl-ODS materials show the largest promise as a transformative LT-ATF cladding material. The extruded 106ZY10C alloy retained 10% total elongation after 16 dpa irradiation and retained 8% total elongation after 50 dpa. Additional challenges with FeCrAl-ODS alloys also remain, including optimization of end cap joining methodologies, enhancement of fracture toughness, scaling production to prove economic viability, and optimizing post-pilger heat treatments to maximize ductility and irradiation resistance.
- Ion irradiations can rapidly get comparative irradiation hardening data to allow for the rapid screening of various long-term ATF candidates, and should be leveraged as a prerequisite to future neutron irradiation campaigns as a valuable accelerated screening tool.

5. REFERENCES

[1] M. Snead *et al.*, "Technology Implementation Plan ATF FeCrAl Cladding for LWR Application," *ORNL/TM-2014-353, Oak Ridge National Laboratory (May 2014),* 2014.

[2] X. Chen, K. G. Field, R. Howard, C. P. Massey, and A. T. Nelson, "Post-Irradiation Fracture Toughness Characterization of Generation II FeCrAl Alloys," in *ASME 2022 Pressure Vessels & Piping Conference*, 2022, vol. Volume 4B: Materials and Fabrication, V04BT06A019, doi: 10.1115/pvp2022-84517. [Online]. Available: https://doi.org/10.1115/PVP2022-84517

[3] P. D. Edmondson *et al.*, "Irradiation-enhanced α′ precipitation in model FeCrAl alloys," *Scripta Materialia,* vol. 116, pp. 112-116, 2016, doi: 10.1016/j.scriptamat.2016.02.002.

[4] K. G. Field and S. A. Briggs, "3.07 - Radiation Effects in FeCrAl Alloys for Nuclear Power Applications," in *Comprehensive Nuclear Materials (Second Edition)*, R. J. M. Konings and R. E. Stoller Eds. Oxford: Elsevier, 2020, pp. 293-306.

[5] K. G. Field, X. Hu, K. C. Littrell, Y. Yamamoto, and L. L. Snead, "Radiation tolerance of neutron-irradiated model Fe–Cr–Al alloys," *Journal of Nuclear Materials,* vol. 465, pp. 746-755, 2015, doi: 10.1016/j.jnucmat.2015.06.023.

[6] K. G. Field, M. A. Snead, Y. Yamamoto, and K. A. Terrani, "Handbook on the Material Properties of FeCrAl Alloys for Nuclear Power Production Applications, ORNL/SPR-2020/1617," 2020.

[7] K. S. Mao *et al.*, "Improved Irradiation Resistance of Accident-Tolerant High-Strength FeCrAl Alloys with Heterogeneous Structures," *Acta Materialia,* 2022, doi: 10.1016/j.actamat.2022.117843.

[8] C. P. Massey *et al.*, "Deconvoluting the Effect of Chromium and Aluminum on the Radiation Response of Wrought FeCrAl Alloys After Low-Dose Neutron Irradiation," *Journal of Nuclear Materials,* vol. 549, 2021, doi: 10.1016/j.jnucmat.2021.152804.

[9] M. P. Brady, J. Magee, Y. Yamamoto, D. Helmick, and L. Wang, "Co-optimization of wrought alumina-forming austenitic stainless steel composition ranges for high-temperature creep and oxidation/corrosion resistance," *Materials Science and Engineering: A,* vol. 590, pp. 101-115, 2014, doi: 10.1016/j.msea.2013.10.014.

[10] B. A. Pint, Y.-F. Su, M. P. Brady, Y. Yamamoto, J. Jun, and M. R. Ickes, "Compatibility of Alumina-Forming Austenitic Steels in Static and Flowing Pb," *Jom,* vol. 73, no. 12, pp. 4016-4022, 2021, doi: 10.1007/s11837-021-04961-y.

[11] B. A. Pint, K. A. Terrani, M. P. Brady, T. Cheng, and J. R. Keiser, "High temperature oxidation of fuel cladding candidate materials in steam–hydrogen environments," *Journal of Nuclear Materials,* vol. 440, no. 1-3, pp. 420-427, 2013, doi: 10.1016/j.jnucmat.2013.05.047.

[12] B. A. Pint, K. A. Terrani, Y. Yamamoto, and L. L. Snead, "Material selection for accident tolerant fuel cladding," *Metallurgical and Materials Transactions E,* vol. 2, no. 3, pp. 190-196, 2015.

[13] S. B. Bell, K. A. Kane, C. P. Massey, L. A. Baldesberger, D. Lutz, and B. A. Pint, "Strength and rupture geometry of un-irradiated C26M FeCrAl under LOCA burst testing conditions," *Journal of Nuclear Materials,* vol. 557, 2021, doi: 10.1016/j.jnucmat.2021.153242.

[14] K. Kane *et al.*, "The response of accident tolerant fuel cladding to LOCA burst testing: A comparative study of leading concepts," *Journal of Nuclear Materials,* Article vol. 574, 2023, Art no. 154152, doi: 10.1016/j.jnucmat.2022.154152.
[15] C. P. Massey, K. A. Terrani, S. N. Dryepondt, and B. A. Pint, "Cladding burst behavior of Fe-based alloys under LOCA," *Journal of Nuclear Materials,* vol. 470, pp. 128-138, 2016.
[16] A. G. Le Coq *et al.*, "Status report on HFIR irradiation of optimized alumina forming alloys," Oak Ridge National Laboratory (ORNL), Oak Ridge, TN (United States), United States, 2024. [Online]. Available: https://www.osti.gov/biblio/2333784
[17] C. P. Massey, S. L. Dryepondt, P. D. Edmondson, K. A. Terrani, and S. J. Zinkle, "Influence of Mechanical Alloying and Extrusion Conditions on the Microstructure and Tensile Properties of Low-Cr ODS FeCrAl Alloys," *Journal of Nuclear Materials,* vol. 512, pp. 227-238, 2018.
[18] A. G. Le Coq, R. H. Howard, K. D. Linton, and K. G. Field, "Design and Thermal Analysis for Irradiation of Tensile Specimens from Wrought, Powder Metallurgy, and Additive Processed Alloys in the HFIR," Oak Ridge National Laboratory (ORNL), Oak Ridge, TN (United States), United States, 2018. [Online]. Available: https://www.osti.gov/biblio/1474529
[19] K. S. Mao *et al.*, "Irradiation-induced amorphization of Fe-Y-based second phase particles in accident-tolerant FeCrAl alloys," *Materialia,* vol. 15, 2021, doi: 10.1016/j.mtla.2021.101016.
[20] C. P. Massey *et al.*, "The effect of Zr on precipitation in oxide dispersion strengthened FeCrAl alloys," *Journal of Nuclear Materials,* vol. 533, 2020, doi: 10.1016/j.jnucmat.2020.152105.
[21] S. Dryepondt, K. A. Unocic, D. T. Hoelzer, C. P. Massey, and B. A. Pint, "Development of low-Cr ODS FeCrAl alloys for accident-tolerant fuel cladding," *Journal of Nuclear Materials,* Article vol. 501, pp. 59-71, 2018, doi: 10.1016/j.jnucmat.2017.12.035.
[22] S. N. Dryepondt, C. P. Massey, and P. D. Edmondson, "2nd Gen FeCrAl ODS Alloy Development For Accident-Tolerant Fuel Cladding," Oak Ridge National Lab.(ORNL), Oak Ridge, TN (United States), 2016.
[23] S. N. Dryepondt, K. A. Unocic, D. T. Hoelzer, and B. A. Pint, "Advanced ODS FeCrAl alloys for accident-tolerant fuel cladding," Oak Ridge National Lab.(ORNL), Oak Ridge, TN (United States), 2014.
[24] C. P. Massey *et al.*, "Microstructure dependent burst behavior of oxide dispersion–strengthened FeCrAl cladding," *Materials & Design,* vol. 234, p. 112307, 2023/10/01/ 2023, doi: https://doi.org/10.1016/j.matdes.2023.112307.
[25] C. P. Massey *et al.*, "Insights from microstructure and mechanical property comparisons of three pilgered ferritic ODS tubes," *Materials and Design,* Article vol. 213, 2022, Art no. 110333, doi: 10.1016/j.matdes.2021.110333.
[26] C. P. Massey *et al.*, "Post irradiation examination of nanoprecipitate stability and α′ precipitation in an oxide dispersion strengthened Fe-12Cr-5Al alloy," *Scripta Materialia,* Article vol. 162, pp. 94-98, 2019, doi: 10.1016/j.scriptamat.2018.10.047.
[27] C. P. Massey, S. N. Dryepondt, P. D. Edmondson, K. A. Terrani, and S. J. Zinkle, "Particle coarsening during oxide dispersion strengthened fecral thin-walled tube fabrication," in *Transactions of the American Nuclear Society*, 2018, vol. 119, pp. 437-439. [Online]. Available: https://www.scopus.com/inward/record.uri?eid=2-s2.0-

85060864732&partnerID=40&md5=b4fb6a059858f50b16830ec1249da54c. [Online]. Available: https://www.scopus.com/inward/record.uri?eid=2-s2.0-85060864732&partnerID=40&md5=b4fb6a059858f50b16830ec1249da54c

[28] C. P. Massey, S. N. Dryepondt, P. D. Edmondson, K. A. Terrani, and S. J. Zinkle, "Influence of mechanical alloying and extrusion conditions on the microstructure and tensile properties of Low-Cr ODS FeCrAl alloys," *Journal of Nuclear Materials,* Article vol. 512, pp. 227-238, 2018, doi: 10.1016/j.jnucmat.2018.10.017.

[29] C. P. Massey *et al.*, "Multiscale investigations of nanoprecipitate nucleation, growth, and coarsening in annealed low-Cr oxide dispersion strengthened FeCrAl powder," *Acta Materialia,* vol. 166, pp. 1-17, 2019, doi: 10.1016/j.actamat.2018.11.062.

[30] M. P. Brady, Y. Yamamoto, M. L. Santella, and L. R. Walker, "Composition, Microstructure, and Water Vapor Effects on Internal/External Oxidation of Alumina-Forming Austenitic Stainless Steels," *Oxidation of Metals,* vol. 72, no. 5, pp. 311-333, 2009/12/01 2009, doi: 10.1007/s11085-009-9161-2.

[31] R. H. Howard, D. Chandler, A. G. Le Coq, S. A. Taller, K. D. Linton, and M. N. Cinbiz, "The state of the art for neutron irradiation experiments from the perspective of the High Flux Isotope Reactor (HFIR)," *Nuclear Engineering and Design,* vol. 444, p. 114401, 2025/12/01/ 2025, doi: https://doi.org/10.1016/j.nucengdes.2025.114401.

[32] P. Champlin *et al.*, "Capsule and Specimen Geometries for HFIR Irradiation Testing Supporting the Transformational Challenge Reactor," Oak Ridge National Laboratory (ORNL), Oak Ridge, TN (United States), 2019.

[33] P. Champlin, C. Massey, A. Le Coq, S. Taller, T. Byun, and K. Linton, "AMMT FY23 HFIR Irradiation Test Matrix–Supported by the Design of a Miniature Bend Bar Irradiation Vehicle," Oak Ridge National Laboratory (ORNL), Oak Ridge, TN (United States), 2023.

[34] A. A. Campbell, W. D. Porter, Y. Katoh, and L. L. Snead, "Method for analyzing passive silicon carbide thermometry with a continuous dilatometer to determine irradiation temperature," *Nuclear Instruments and Methods in Physics Research Section B: Beam Interactions with Materials and Atoms,* vol. 370, pp. 49-58, 2016/03/01/ 2016, doi: https://doi.org/10.1016/j.nimb.2016.01.005.

[35] K. G. Field, J. L. McDuffee, J. W. Geringer, C. M. Petrie, and Y. Katoh, "Evaluation of the continuous dilatometer method of silicon carbide thermometry for passive irradiation temperature determination," *Nuclear Instruments and Methods in Physics Research Section B: Beam Interactions with Materials and Atoms,* vol. 445, pp. 46-56, 2019/04/15/ 2019, doi: https://doi.org/10.1016/j.nimb.2019.02.022.

[36] *E1820 − 25a: Standard Test Method for Measurement of Fracture Toughness*, ASTM International, 2025.

[37] R. W. Hertzberg, R. P. Vinci, and J. L. Hertzberg, *Deformation and fracture mechanics of engineering materials*. John Wiley & Sons, 2020.

[38] B. A. Pint, "Optimization of reactive-element additions to improve oxidation performance of alumina-forming alloys," *Journal of the American Ceramic Society,* vol. 86, no. 4, pp. 686-95, 2003.

[39] S. K. Lee *et al.*, "BISON validation of FeCrAl cladding mechanical failure during simulated reactivity-initiated accident conditions," *Journal of Nuclear Materials,* Article vol. 564, 2022, Art no. 153676, doi: 10.1016/j.jnucmat.2022.153676.

[40] N. R. Brown, B. E. Garrison, R. R. Lowden, M. N. Cinbiz, and K. D. Linton, "Mechanical failure of fresh nuclear grade iron–chromium–aluminum (FeCrAl) cladding under simulated hot zero power reactivity initiated accident conditions," *Journal of Nuclear Materials,* vol. 539, 2020, doi: 10.1016/j.jnucmat.2020.152352.

[41] K. Farrell, T. S. Byun, and N. Hashimoto, "Deformation mode maps for tensile deformation of neutron-irradiated structural alloys," *Journal of Nuclear Materials,* vol. 335, no. 3, pp. 471-486, 2004, doi: 10.1016/j.jnucmat.2004.08.006.

[42] T. S. Byun, J. W. Werden, T. G. Lach, N. G. Russell, A. G. Le Coq, and K. D. Linton, "Strength and ductility of additively manufactured 316L stainless steel: Impact of neutron irradiation and data variability," *Journal of Nuclear Materials,* vol. 615, p. 155956, 2025/09/01/ 2025, doi: https://doi.org/10.1016/j.jnucmat.2025.155956.

[43] S. Zinkle and N. Ghoniem, "Operating temperature windows for fusion reactor structural materials," *Fusion Engineering and design,* vol. 51, pp. 55-71, 2000.

[44] K. G. Field and R. H. Howard, "Status of FeCrAl ODS Irradiations in the High Flux Isotope Reactor," Oak Ridge National Lab.(ORNL), Oak Ridge, TN (United States). High Flux …, 2016.

[45] K. G. Field, C. P. Massey, K. R. Smith, S. A. Briggs, D. Zhang, and K. C. Littrell, "Shielded magnetic small-angle neutron scattering for characterization of radioactive samples," *Applied Crystallography,* vol. 58, no. 3, pp. 1000-1014, 2025.

[46] C. P. Massey *et al.*, "Insights from microstructure and mechanical property comparisons of three pilgered ferritic ODS tubes," *Materials & Design,* vol. 213, 2022, doi: 10.1016/j.matdes.2021.110333.

[47] W. D. Nix and H. Gao, "Indentation size effects in crystalline materials: a law for strain gradient plasticity," *Journal of the Mechanics and Physics of Solids,* vol. 46, no. 3, pp. 411-425, 1998.